A QCD ANALYSIS OF HIGH ENERGY NEUTRINO-NUCLEON INTERACTIONS

A THESIS SUBMITTED TO
THE GRADUATE SCHOOL OF NATURAL AND APPLIED SCIENCES
OF
THE MIDDLE EAST TECHNICAL UNIVERSITY

BY

HALİL GAMSIZKAN

IN PARTIAL FULFILLMENT OF THE REQUIREMENTS FOR THE DEGREE OF

MASTER OF SCIENCE

IN

THE DEPARTMENT OF PHYSICS

SEPTEMBER 2003

Approval of the Graduate School of Natural and Applied Sciences.

Prof. Dr. Canan Özgen
Director

I certify that this thesis satisfies all the requirements as a thesis for the degree of Master of Science.

Prof. Dr. Sinan Bilikmen
Head of Department

This is to certify that we have read this thesis and that in our opinion it is fully adequate, in scope and quality, as a thesis for the degree of Master of Science.

Assoc. Prof. Dr. Meltem Serin
Supervisor

Examining Committee Members

Prof. Dr. A. Ulvi Yılmazer

Prof. Dr. Mehmet Zeyrek

Assoc. Prof. Dr. Meltem Serin

Assoc. Prof. Dr. Gürsevil Turan

Assoc. Prof. Dr. Yusuf İpekoğlu

ABSTRACT

A QCD ANALYSIS OF HIGH ENERGY NEUTRINO-NUCLEON INTERACTIONS

Gamsızkan, Halil

MS.Sci., Department of Physics

Supervisor: Assoc. Prof. Dr. Meltem Serin

September 2003, 65 pages

In this thesis, a leading-order QCD analysis of structure functions in neutrino-nucleon interactions is performed. From the CCFR nucleon structure function data, the QCD parameter Lambda has been extracted. This measurement also corresponds to a measurement of the strong coupling constant. Two fits to the data have been performed, the nonsinglet-only fit and the singlet-nonsinglet combined fit. The result for Lambda was found to be $289\,^{+62}_{-59} \pm 76$ MeV, where the errors are statistical and systematical, respectively. This result is compared to the world-wide measurements of this quantity. In order to verify the agreement, also the logarithmic slopes of the QCD model and the structure function data are calculated and compared.

Keywords: Structure Function, Strong Coupling Constant, QCD Parameter Lambda

ÖZ

YÜKSEK ENERJİLİ NÖTRİNO-NÜKLEON ETKİLEŞİMLERİNİN QCD ANALİZİ

Gamsızkan, Halil

Yüksek Lisans, Fizik Bölümü

Tez Yöneticisi: Assoc. Prof. Dr. Meltem Serin

Eylül 2003, 65 sayfa

Bu tezde, nötrino-nükleon etkileşimlerinden elde edilmiş nükleon yapı fonksiyonlarının bir ana-mertebe QCD analizi yapılmaktadır. CCFR nükleon yapı fonksiyonu verisi kullanılarak, QCD parametresi Lambda hesaplanmıştır. Bu ölçüm aynı zamanda bir güçlü bağlaşım sabiti ölçumüne karşılık gelmektedir. Deney verisine iki fit yapılmıştır, sadece-nonsinglet fit ve singlet-nonsinglet birleşik fit. Lambda ölçüm sonucu, verilen hatalar sırasıyla istatistiksel ve sistematik olmak üzere, $289\,^{+62}_{-59} \pm 76$ MeV olarak bulunmuştur. Bu sonuç Lambda'nın önceden yapılmış olan ölçümleri ile kıyaslanmıştır. QCD modeli ile yapı fonksiyonu verisi uyuşumunun bir kontrolü olarak logaritmik eğimler hesaplanmış ve kıyaslanmıştır.

Anahtar Kelimeler: Yapı Fonksiyonları, Güçlü bağlaşım sabiti, QCD Parametresi Lambda

To my family...

TABLE OF CONTENTS

LIST OF TABLES

LIST OF FIGURES

CHAPTER 1

INTRODUCTION

Scattering particles off nuclei is a well-proved way of probing the internal structure of nucleons and testing the physical theories governing their structure. Nucleons can be bombarded by beams of high-energy particles (such as leptons) and from the nature of this scattering nucleon structure functions, which describe the composite structure of nucleons can be measured. The nature of lepton-nucleon scattering is well understood in the context of the Standard Model of electro-weak and strong interactions.

It's been understood that the nucleons are composed of pointlike particles called quarks. Quarks inside nucleons undergo strong interactions which is described by the theory of Quantum Chromodynamics (QCD). What QCD predicts about the nucleon structure functions is not the structure functions themselves, but their dependence on the probing 'depth'*. Therefore, by comparing the structure function data of different nucleon 'depth', we may check whether QCD is valid, and if so, we may measure some fundamental parameters of QCD that are not predicted by the theory, such as the strong coupling constant α_s.

*Uncertainty principle states that in order to resolve nucleon constituents (quarks) via deep inelastic scattering, one needs a mediator boson of the particular interaction whose wavelength must be much less than the nucleons' radius: $\lambda(\approx 1/\sqrt{-q^2}) \ll 1\,\mathrm{Fm}$. Here q

The content of this thesis is a measurement of the QCD parameter Λ, via the CCFR experiment structure function measurements; which also corresponds to a measurement of the strong coupling constant α_s. CCFR experiment measured nucleon structure functions via the charged-current scattering of muon neutrinos and antineutrinos on the nucleons of an iron target.

1.1 Charged-Current Neutrino-Nucleon Scattering

According to the Standard Model, neutrinos are elementary particles with unique properties. They are approximately massless spin 1/2 fermions which have no charge and no magnetic moment. Neutrinos interact with matter only via the weak-interaction. All the neutrinos are left-handed while all the anti-neutrinos are right-handed.

Weak interactions are classified as the neutral-current (NC) and the charged-current (CC) interactions. CC interactions are mediated by charged $W^{\pm}$ bosons, while NC interactions are mediated by electrically neutral Z bosons. A CC reaction transforms a neutrino into it's corresponding charged lepton, and vice versa.

The nucleon structure functions analyzed in this study are measured from the reactions of muon-neutrino (ν_μ) and antineutrinos ($\overline{\nu}_\mu$) with nucleons of an iron target:

$$\nu_\mu + N \rightarrow \mu^- + X,$$
$$\overline{\nu}_\mu + N \rightarrow \mu^+ + X,$$

where N is the target nucleon, $\mu^{\mp}$ is a muon with negative (positive) charge and X is the hadronic final state. The energy and momentum of the neutrino, the outgoing muon, the target nucleon and the hadronic final state are represented by the four-vectors k, k', p, p', respectively, see Fig. 1.1. Here, the four-momentum transferred to the nucleon is represented by q, which is defined

represents the four-momentum transferred to the nucleon.

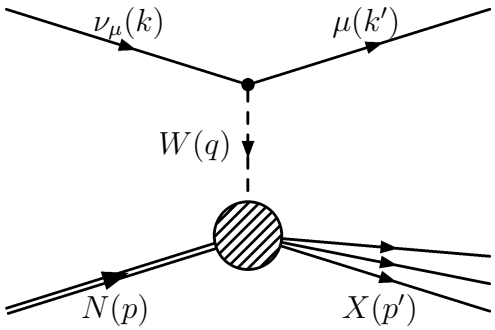

Figure 1.1: Leading order Feynman diagram representing the deep inelastic neutrino-nucleon charged-current scattering.

as:

$$q = k - k' = p' - p. \tag{1.1}$$

For moderate values of energy transfer, the target nucleon is left intact after the reaction; such reactions are called *quasi-elastic* reactions. On the other hand, if the transferred energy is too high, the nucleon loses it's identity and breaks up in the reaction, and the final state consists of a shower of hadronic particles. Such reactions are called *deep-inelastic scattering* (DIS).

1.1.1 Kinematic formalism

Experimentally measured quantities of neutrino DIS in the CCFR experiment are the scattering angles and the four-momentum of the outgoing muon θ_μ, ϕ_μ, p_μ and the total energy of the hadronic final state $E_{\rm had}$. Such a study in which only the total energy of the hadronic final state is measured is called an inclusive study, unlike an exclusive study, in which all the particles in the hadronic final state are measured individually.

The energy-momentum four vectors of the incoming neutrino, the outgoing muon and the target nucleon can be written in the laboratory frame in terms

of the experimentally measured quantities:

$$k = (E_\nu, 0, 0, E_\nu), \tag{1.2}$$

$$k' = (E_\mu, \mathbf{p}_\mu \sin\theta_\mu \cos\phi_\mu, \mathbf{p}_\mu \sin\theta_\mu \sin\phi_\mu, \mathbf{p}_\mu \cos\theta_\mu), \tag{1.3}$$

$$p = (M_N, 0, 0, 0), \tag{1.4}$$

where E_ν is the energy of the incoming neutrino, E_μ is the energy of the outgoing muon and M_N is the mass of the struck nucleon. A number of invariant variables convenient to describe DIS can be constructed from these four-momenta:
The square of the center of mass energy:

$$s = (p + k)^2, \tag{1.5}$$

the energy transferred to the nucleon:

$$\nu = \frac{p \cdot q}{M_N}, \tag{1.6}$$

the invariant mass of the hadronic final state:

$$W^2 = (p + q)^2, \tag{1.7}$$

the negative square of the four-momentum transfer:

$$Q^2 = -q^2, \tag{1.8}$$

the Björken scaling variables, which represent the fraction of the parent nucleon's four momentum carried by the struck parton:

$$x = \frac{Q^2}{2p \cdot q}, \tag{1.9}$$

and the inelasticity:

$$y = \frac{p \cdot q}{p \cdot k}. \tag{1.10}$$

Using the expressions (1.2-1.4), these variables can be rewritten in terms of the laboratory system variables p_μ, θ_μ and $E_{\rm had}$:

$$s = M_N^2 + 2M_N E_\nu, \tag{1.11}$$

$$\nu = E_\nu - E_\mu = E_{\rm had}, \tag{1.12}$$

$$W^2 = M_N^2 - Q^2 + 2M_N\nu\,, \tag{1.13}$$

$$Q^2 = 2E_\nu(E_\mu - p_\mu\cos\theta_\mu) - m_\mu^2 \;\simeq\; 4E_\nu p_\mu \sin^2\frac{1}{2}\theta_\mu\,, \tag{1.14}$$

$$x = \frac{Q^2}{2\nu M_N}, \tag{1.15}$$

$$y = \frac{\nu}{\nu + E_\mu}. \tag{1.16}$$

1.1.2 Neutrino-nucleon deep inelastic scattering cross-section

The scattering cross-section is proportional to the squared matrix element $|\mathcal{M}|^2$, which contains the heart of the physics of the interaction. For charged-current interactions, in the tree level (single W exchange approximation), the squared matrix element can be written as:

$$\mathrm{d}\sigma \sim |\mathcal{M}|^2 = \frac{2G_F^2}{(1+Q^2/M_W^2)^2} L_{\alpha\beta}W^{\alpha\beta}, \tag{1.17}$$

where G_F is the Fermi weak coupling constant, $L_{\alpha\beta}$ and $W^{\alpha\beta}$ are two tensors describing the leptonic and hadronic vertices respectively (see Fig. 1.1) and M_W is the mass of the W boson mediating the interaction. It may be shown that the leptonic tensor is:

$$\begin{aligned} L_{\alpha\beta} &= [\bar{u}(k)\gamma_\alpha(1-\gamma_5)u(k')]\,[\bar{u}(k')\gamma_\beta(1-\gamma_5)u(k)] \\ &= 8[k'_\alpha k_\beta + k'_\beta k_\alpha - (k\cdot k' - m_\mu^2)\,g_{\alpha\beta} \mp i\,\epsilon_{\alpha\beta\gamma\delta}\,k^\gamma k'^\delta], \end{aligned} \tag{1.18}$$

where $\epsilon_{\alpha\beta\gamma\delta}$ is the totally antisymmetric tensor.

The nucleon having an *a priori* unknown composite nature requires that we must construct the hadronic tensor to the most general form, also introducing functions to describe the nucleon's inner structure. Hence the hadronic tensor is constructed out of the two independent variables of the hadronic vertex p

and q, the identity matrix, and the introduced neutrino-nucleon scattering 'W' structure functions. The resultant form is written as follows [1]:

$$W^{\alpha\beta} = -\, g^{\alpha\beta} W_1 + \frac{p^\alpha p^\beta}{M_N^2} W_2 - \frac{i\,\epsilon^{\alpha\beta\gamma\delta}\, p_\gamma\, q_\delta}{2M_N^2} W_3. \tag{1.19}$$

The W_3 structure function is specific to weak interactions, i.e. there is no electromagnetic counterpart of the W_3 structure function. The structure functions are functions of two variables, which are usually taken to be ν and Q^2.

The W_i are conventionally written as traditional dimensionless structure functions F_i:

$$MW_1(\nu, Q^2) \rightarrow F_1(x, Q^2), \tag{1.20}$$

$$\nu W_2(\nu, Q^2) \rightarrow F_2(x, Q^2), \tag{1.21}$$

$$\nu W_3(\nu, Q^2) \rightarrow F_3(x, Q^2). \tag{1.22}$$

By using equations (1.17-1.22), the differential cross-section of neutrino-nucleon charged-current deep inelastic scattering can be written in terms of the variables x, y and Q^2 as following:

$$\begin{aligned} \frac{\mathrm{d}^2\sigma^{\nu(\bar{\nu})}}{\mathrm{d}x\,\mathrm{d}y} =& \frac{G_F^2 M_N E_\nu}{\pi(1+Q^2/M_W^2)^2} \times \\ & \left[\frac{1}{2}y^2 \cdot 2xF_1 + \left(1 - y - \frac{M_N x y}{2E_\nu}\right)F_2 \pm \left(y - \frac{1}{2}y^2\right)xF_3\right], \end{aligned} \tag{1.23}$$

where +(-) corresponds to the neutrino(antineutrino) scattering cross-section. Here the Q^2/M_W^2 term can be taken to be zero, since in the kinematic domain of the CCFR experiment $Q^2 \ll M_W^2 \approx (80\ \mathrm{GeV})^2$. The nucleon structure functions can be measured via DIS experiments and an understanding of them is essential to an understanding of the nucleon structure.

1.1.3 Partons

Early nucleon structure function measurements provided two important observations about the structure functions [2]:

1. Q^2 dependence of structure functions is weak, and

2. to a good approximation, the Callan-Gross relation [3]

$$2xF_1(x) = F_2(x) \tag{1.24}$$

holds.

Weak dependence of nucleon structure functions on Q^2 can be understood in terms of elastic scattering of neutrinos off pointlike nucleon constituents. In principle, if point-like particles reside inside the nucleon, we should be able to observe them with a small-wavelength (i.e. large Q^2) virtual boson. When we get to the depth that the scattering is over the point-like constituent, the structure functions should become the 'point structure functions'

$$2MW_1^{\text{Point}}(\nu, Q^2) = \frac{Q^2}{2M\nu}\delta\left(1 - \frac{Q^2}{2M\nu}\right), \tag{1.25}$$

$$\nu W_2^{\text{Point}}(\nu, Q^2) = \delta\left(1 - \frac{Q^2}{2M\nu}\right), \tag{1.26}$$

$$\nu W_3^{\text{Point}}(\nu, Q^2) = \frac{Q^2}{2M\nu}\delta\left(1 - \frac{Q^2}{2M\nu}\right). \tag{1.27}$$

Note that in this domain of high Q^2, the point structure functions are functions of a single dimensionless quantity $Q^2/2M\nu$.

That W_i are finite functions and depend only on the variable x and not on Q^2 for the

$$\begin{aligned} Q^2 &\to \infty\,, \\ \nu &\to \infty \end{aligned} \tag{1.28}$$

limit is called Björken scaling [4]. Björken scaling phenomenon is the primary indication of the composite nature of hadrons. Nucleon constituents which we resolve via DIS are called *partons*.

The validity of Callan-Gross relation, eq. (1.24), indicates that the partons are spin 1/2 particles. Callan-Gross relation is explained by the vanishing of the longitudinally polarized virtual boson-parton scattering cross-section. For spin 1/2 massless particles, such an interaction violates the helicity conservation. As

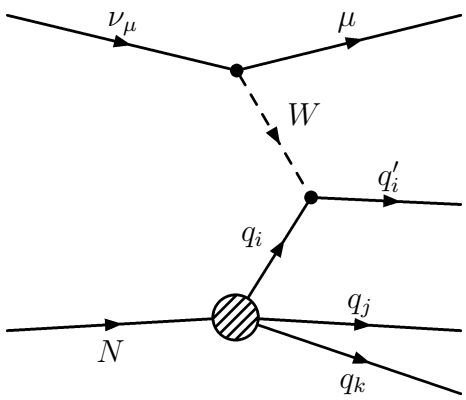

Figure 1.2: Neutrino-parton scattering.

a consequence of the Björken scaling phenomenon, and the validity of Callan-Gross relation to a good approximation[†], we identify the spin 1/2 point-like nucleon constituents as *quarks*.

The composite nature of nucleons is explained by the quark-parton model [5]. Parton model analyzes the scattering in the Breit frame[‡], in which the target proton (and the constituent partons) move with infinite, purely longitudinal momentum. The parton absorbs the incoming virtual boson and recoils in the backward direction; its momentum still being longitudinal. As the momentum of the nucleon is assumed to be infinite, the interaction time scale of the constituent quarks is much longer than the time scale of the collusion, hence the struck quark is almost free, and the scattering is incoherent, see Fig. 1.2.

In the quark-parton model, partons are assumed to carry a fraction x of the parent nucleon's four-momentum p^μ. However, due to the dynamical processes in the nucleon, quarks do not have a fixed four-momentum. This is described by the quark distribution functions $q(x)$, where $q(x)\mathrm{d}x$ is the probability of finding a quark of flavor q in a hadron, which carries a fraction x to $x + \mathrm{d}x$ of the parent hadron's four-momentum p^μ. $q(x)$ may be the $u(x)$, $d(x)$, $s(x)\ldots$ quark distributions, while $\bar{q}(x)$ are the corresponding antiquark distributions.

[†] Violations of the Callan-Gross relation are described at the end of this section.
[‡] also called the *brick wall frame.*

According to the static quark model, nucleons are composed of three quarks: the proton has two u and one d, while the neutron has one u and two d quarks. These quarks constitute the *valence quark* content of the nucleon, and are described by the $q_v(x)$ distributions. Since the proton and the neutron are members of an isospin doublet, their quark contents are related. For instance, there are as many u quarks in a proton as d quarks in a neutron. As a convention, quark distributions are defined by the proton quark distributions:

$$u(x) \equiv u^p(x) = d^n(x), \tag{1.29}$$

$$d(x) \equiv d^p(x) = u^n(x), \tag{1.30}$$

where the superscript 'p' represents a proton quark distribution while 'n' represents a neutron quark distribution.

Experimental results show that, only (approximately) half of the nucleon momentum is occupied by quarks. The missing half of the momentum is assumed to be occupied by the *gluons*, which are the mediators of the strong interaction. Gluon decays into quark-antiquark pairs affect the quark content of the nucleon. By this mechanism, for example, antiquarks and quarks with flavors other than u and d may happen to exist in the nucleon. Quarks created by such processes constitute the *sea quark* content of the nucleon and are described by the $q_s(x)$ distribution functions. Hence, the overall quark content of the nucleon is determined by the valence quark content and the contribution from the sea quarks:

$$u(x) = u_v(x) + u_s(x), \tag{1.31}$$

$$d(x) = d_v(x) + d_s(x), \tag{1.32}$$

$$u_s(x) = \bar{u}_s(x) = d_s(x) = \bar{d}_s(x) = s_s(x) = \bar{s}_s(x), \tag{1.33}$$

where a symmetric sea is assumed.

It is convenient to express the quark distributions in flavor combinations. The flavor singlet and nonsinglet distributions are defined as:

$$q^S = \sum_i (q_i + \bar{q}_i), \tag{1.34}$$

$$q^{NS} = \sum_i (q_i - \bar{q}_i) = \sum_i q_v. \tag{1.35}$$

To establish a connection between the parton model and the nucleon structure functions, we need to write down the parton model analog of the neutrino-nucleon cross-sections (1.23). We set out by writing the differential cross-section of neutrino-free quark scattering [1]:

$$\frac{\mathrm{d}\sigma^{\nu q}}{\mathrm{d}y} = \frac{\mathrm{d}\sigma^{\bar{\nu}\bar{q}}}{\mathrm{d}y} = \frac{G_F^2 s_{\nu q}}{\pi}, \tag{1.36}$$

$$\frac{\mathrm{d}\sigma^{\nu \bar{q}}}{\mathrm{d}y} = \frac{\mathrm{d}\sigma^{\bar{\nu} q}}{\mathrm{d}y} = \frac{G_F^2 s_{\nu q}}{\pi}(1-y)^2, \tag{1.37}$$

where $s_{\nu q}$ is the center of mass energy of the neutrino-quark system, which is $s_{\nu q} = x s_{\nu N}$. The factor $(1-y)^2$ describes the suppression of the scattering cross-section in weak interactions in two states of opposite helicity.

The incoherent scattering assumption of parton model states that the neutrino-nucleon DIS cross-section can be written as an incoherent sum of individual neutrino-parton scattering cross-sections. These cross-sections are weighed by the parton distribution functions:

$$\frac{\mathrm{d}\sigma(\nu N \to \mu X)}{\mathrm{d}x\,\mathrm{d}y} = \sum_i \left[q_i(x) \frac{\mathrm{d}\sigma_i}{\mathrm{d}y} + \bar{q}_i(x) \frac{\mathrm{d}\bar{\sigma}_i}{\mathrm{d}y} \right]. \tag{1.38}$$

Hence, we write the (anti)neutrino-nucleon scattering cross-section in terms of the quark distribution functions as follows:

$$\frac{\mathrm{d}^2\sigma^{\nu}}{\mathrm{d}x\,\mathrm{d}y} = \frac{G_F^2 M_N E_\nu}{\pi} \Big[x q(x) + x\bar{q}(x)(1-y)^2 \Big], \tag{1.39}$$

$$\frac{\mathrm{d}^2\sigma^{\bar{\nu}}}{\mathrm{d}x\,\mathrm{d}y} = \frac{G_F^2 M_N E_\nu}{\pi} \Big[x q(x)(1-y)^2 + x\bar{q}(x) \Big]. \tag{1.40}$$

By comparing the above cross-sections with the cross-sections (1.23) we obtain the definitions of the nucleon structure functions in terms of the quark

distributions:

$$2xF_1 = F_2 = 2x \sum_i (q_i + \bar{q}_i) \tag{1.41}$$

and

$$xF_3 = 2x \sum_i (q_i - \bar{q}_i). \tag{1.42}$$

In charged-current weak interactions, charge conservation at the interaction vertex dictates that the neutrinos scatter only off negatively charged quarks d, $\bar{u}$, s and $\bar{c}$, while the antineutrinos scatter only off positively charged quarks $\bar{d}$, u, $\bar{s}$ and c. The third family quarks are too heavy to be considered in the energy range of the experimental data analyzed in this study. Therefore, for (anti)neutrino-nucleon CC interactions, equations (1.41) and (1.42) become:

$$2xF_1^{\nu} = F_2^{\nu} = 2x(d + \bar{u} + s + \bar{c}), \tag{1.43}$$

$$2xF_1^{\bar{\nu}} = F_2^{\bar{\nu}} = 2x(\bar{d} + u + \bar{s} + c), \tag{1.44}$$

$$xF_3^{\nu} = 2x(d - \bar{u} + s - \bar{c}), \tag{1.45}$$

$$xF_3^{\bar{\nu}} = 2x(-\bar{d} + u - \bar{s} + c). \tag{1.46}$$

It is customary to define the isoscalar neutrino structure functions $2xF_1^N$, F_2^N and xF_3^N, which are the averages of the proton and the neutron structure functions $(F_i^{\nu p} + F_i^{\nu n})/2$:

$$\begin{aligned} 2xF_1^{\nu N} = F_2^{\nu N} = 2xF_1^{\bar{\nu} N} = F_2^{\bar{\nu} N} &= x(u + \bar{u} + d + \bar{d} + s + \bar{s} + c + \bar{c}) \\ &\equiv xq^S, \end{aligned} \tag{1.47}$$

$$xF_3^{\nu N} = x(u - \bar{u} + d - \bar{d} + 2s - 2\bar{c}), \tag{1.48}$$

$$xF_3^{\bar{\nu} N} = x(u - \bar{u} + d - \bar{d} - 2s + 2c). \tag{1.49}$$

In this study, average of the xF_3 structure function data obtained from neutrino and antineutrino scattering is analyzed. Note that the averaged structure function corresponds to the valence quark distribution:

$$xF_3 = \frac{xF_3^{\nu N} + xF_3^{\bar{\nu} N}}{2} = xu_v + xd_v = x \sum q_v \equiv xq^{NS}. \tag{1.50}$$

Although the Callan-Gross relation is known to agree well with the experimental data, it's been observed that this relation is not exact. The violations are due to the longitudinal cross-section σ_L being nonzero. The violations are expressed in terms of the R parameter which is the ratio of the longitudinal and transverse cross-sections σ_L/σ_T:

$$R = \left(1 + \frac{4M_N^2 x^2}{Q^2}\right)\frac{F_2}{2xF_1} - 1. \tag{1.51}$$

Note that, in the $Q^2 \to \infty$ limit and for $R \to 0$ the Callan-Gross relation becomes exact.

1.2 Quantum Chromodynamics

Quark-gluon dynamics, namely the strong interactions are described by the non-Abelian gauge theory of Quantum Chromodynamics. QCD assumes that, all quarks carry color degrees of freedom, which acts as charge acts in QED: It's the source of the interaction. Three possible states of the color degree of freedom are conventionally named as red, green and blue.

The mediators of strong interaction are spin-1 massless gluons. In QCD, color charge is exchanged between colored particles by gluons, so gluons *do* carry color charge, which indeed is a property of non-Abelian gauge theories. A consequence of this is that, unlike the mediator photons of QED, gluons can interact with other gluons. More technically, QCD has three and four gluon interaction vertices, which has no analogue in QED. This availability is accounted for a characteristic feature of QCD: Asymptotic freedom.

Asymptotic freedom states that, as the distance between two quarks diminishes so does the effective strength of their interaction; and the particles become asymptotically free. On the other hand, as the distance between quarks increases, so does the effective interaction strength. Asymptotic freedom explains the absence of observed free quarks.

1.2.1 Running coupling constant

It's the distinction between a coupling and an *effective* coupling which underlies the concept of a running coupling constant.

Both in QED and QCD, when perturbatively calculating cross-sections, the inclusion of higher-order diagrams leads to divergent terms. These infinities are treated in a systematic way by the renormalization technique. Renormalization involves introducing a free parameter, the renormalization scale μ^2, which has the dimension of mass. The now-finite divergent terms evaluated at the scale μ are absorbed into a redefinition of the coupling, *the effective coupling*. Hence a particle is said to be interacting with an effective coupling. The additional diagrams whose divergent terms are absorbed into the effective coupling contains creation and annihilation of virtual particles such as electrons and quarks, hence we may picturise the situation as following: Electromagnetic interactions see electrons which are surrounded by a cloud of e^-e^+ pairs, and strong interactions see quarks surrounded by a cloud of $q\bar{q}$ pairs. So the effective coupling depends on the distance scale between the interacting particles. For the QED case this cloud seems to screen the charge of a particle. For the long distance limit $Q^2 \to 0$, we observe the charge e, however when we get to closer distances, the effective coupling is expected to increase as the screening effect will decrease.

However, in the QCD case the screening seems to be in the opposite way. It's understood that the gluon splitting ($g_0 \to g_1 + g_2$) *antiscreens* the color charge. Roughly speaking, a splitting gluon spreads the color charge away, leaving less charge for the short distance interactions. Hence, in the far observation limit, coupling tends to infinity and while we get to smaller distance scales, coupling diminishes and the quarks become asymptotically free.

In the leading logarithmic approximation, the effective coupling, or the running coupling constant of QCD is written as [6]:

$$\alpha_s(Q^2) = \frac{\alpha_s(\mu^2)}{1 + \frac{\alpha_s(\mu^2)}{12\pi}(33 - 2n_f)\ln\left(\frac{Q^2}{\mu^2}\right)}, \tag{1.52}$$

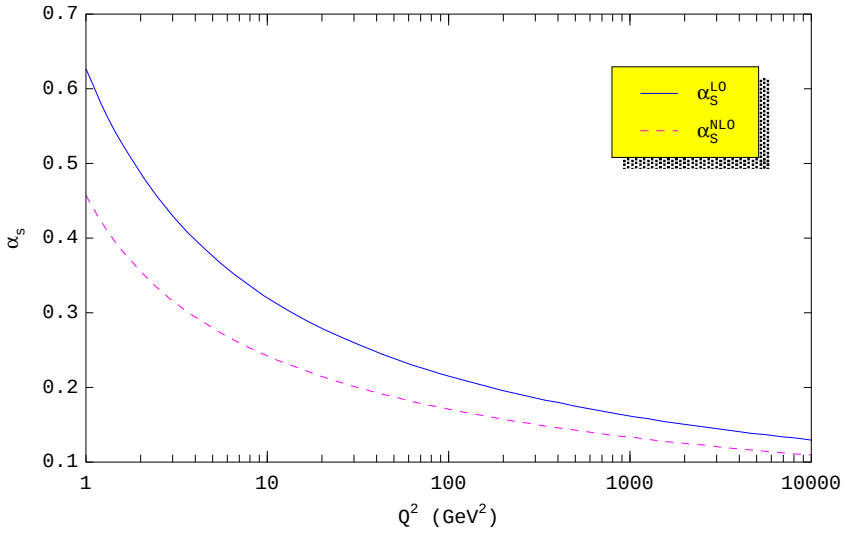

Figure 1.3: $\alpha_s(Q^2)$ plotted for $\Lambda = 300$ MeV. Dashed line represents the next to leading-order running coupling constant.

here μ is the renormalization scale and n_f is the number of quark flavors participating in the interaction at the given Q^2 scale. For $n_f \leq 16$, the denominator of (1.52) is positive and the running coupling constant decreases logarithmically with increasing Q^2 (or decreasing distance), in consistence with asymptotic freedom.

With the definition of the parameter Λ

$$\Lambda^2 = \mu^2 \exp\left[\frac{-12\pi}{(33-2n_f)\alpha_s(\mu^2)}\right], \tag{1.53}$$

which has the dimension of mass, equation (1.52) becomes

$$\alpha_s(Q^2) = \frac{12\pi}{(33-2\,n_f)\ln(\frac{Q^2}{\Lambda^2})}. \tag{1.54}$$

Note that as $Q^2 \sim \Lambda^2$ the denominator of (1.54) becomes zero and $\alpha_S(Q^2)$ tends to infinity. When α_S is too large, the strong interaction becomes too strong to be described by the perturbative approach. Hence we can think of Λ as the distance scale at which ‘strong interaction becomes very strong’. It sets the lower bound of the perturbative region, drawing a border between the nucleon’s internal world of perturbatively interacting quarks, and the world of pions, neutrons, etc.

1.2.2 Evolution equations

In perturbative QCD (PQCD), scaling violations are described by the Altarelli-Parisi (AP) evolution equations [7]:

$$\frac{\mathrm{d}q^{NS}(x,Q^2)}{\mathrm{d}\ln Q^2} = \frac{\alpha_s(Q^2)}{2\pi}\int_x^1 \frac{\mathrm{d}y}{y} q^{NS}(y,Q^2)P_{qq}(x/y), \tag{1.55}$$

$$\frac{\mathrm{d}q^{S}(x,Q^2)}{\mathrm{d}\ln Q^2} = \frac{\alpha_s(Q^2)}{2\pi}\int_x^1 \frac{\mathrm{d}y}{y} \left[q^{S}(y,Q^2)P_{qq}(x/y) + G(y,Q^2)P_{qG}(x/y)\right], \tag{1.56}$$

$$\frac{\mathrm{d}G(x,Q^2)}{\mathrm{d}\ln Q^2} = \frac{\alpha_s(Q^2)}{2\pi}\int_x^1 \frac{\mathrm{d}y}{y} \left[q^{S}(y,Q^2)P_{Gq}(x/y) + G(y,Q^2)P_{GG}(x/y)\right], \tag{1.57}$$

where $\alpha_s(Q^2)$ is the strong coupling constant, q^S and q^{NS} are respectively the singlet and the nonsinglet quark distributions, $P_{qq}, P_{qG}, P_{Gq}, P_{GG}$ are the splitting functions and $G(x,Q^2)$ is the gluon momentum distribution function. Note that equations (1.55-1.57) do not predict $F_i(x,Q^2)$ directly but predict how a given $F_i(x,Q_0^2)$ evolves to a different Q^2 scale, where Q_0^2 is some reference scale.

In an attempt to understand the physical meaning of the splitting functions, let's consider P_{qq} for example. Equation (1.55) can be rewritten in the following form:

$$\begin{aligned} &q^{NS}(x,Q^2) + \mathrm{d}q^{NS}(x,Q^2) = \\ &\quad \int_0^1 \mathrm{d}y \int_0^1 \mathrm{d}z\, \delta(zy-x)\, q^{NS}(y,Q^2) \left[\delta(z-1) + \frac{\alpha}{2\pi}P_{qq}(z)\,\mathrm{d}\ln(Q^2)\right], \end{aligned} \tag{1.58}$$

where $z = x/y$. This new form reveals the meaning of P_{qq}. Given a quark with momentum fraction y, there is a chance that it reduces it's momentum from y to x by radiating a gluon. Hence, the following expression represents the probability density of finding a quark with momentum fraction z inside another, 'parent' quark (or simply the probability density of gluon bremsstrahlung by a quark):

$$\mathcal{P}_{qq} + \mathrm{d}\mathcal{P}_{qq} = \delta(z-1) + \frac{\alpha}{2\pi}P_{qq}(z)\,\mathrm{d}\ln(Q^2). \tag{1.59}$$

Since the total number of quarks minus antiquarks is conserved, the probability of finding a quark inside another quark integrated over all z values must add

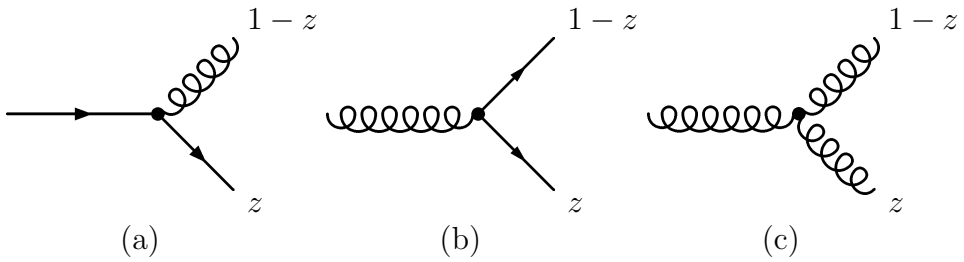

Figure 1.4: Vertices relevant to parton splitting functions: (a) Quark-gluon vertex which determines P_{qq} and P_{Gq}. (b) Gluon annihilation into $q\bar{q}$ pair vertex which determines P_{qG}. (c) Three gluon vertex which determines P_{GG}.

up to one. This requires that:

$$\int_0^1 P_{qq}(z)\,\mathrm{d}z = 0. \tag{1.60}$$

The meanings of other splitting functions follow that of P_{qq}, see Fig. 1.4. Momentum conservation at the interaction vertices impose constraints on the P functions. For $z < 1$ we have:

$$P_{qq}(z) = P_{Gq}(1-z), \tag{1.61}$$

$$P_{qG}(z) = P_{qG}(1-z), \tag{1.62}$$

$$P_{GG}(z) = P_{GG}(1-z) \tag{1.63}$$

since, when a quark emits a gluon, it's momentum fraction becomes z, hence the emitted gluon's fraction will be $(1-z)$, and so on.

Explicitly, the leading-order splitting functions are written as:

$$P_{qq}(z) = \frac{4}{3}\frac{1+z^2}{(1-z)_+} + 2\delta(1-z), \tag{1.64}$$

$$P_{Gq}(z) = \frac{4}{3}\frac{1+(1-z)^2}{z}, \tag{1.65}$$

$$P_{qG}(z) = \frac{1}{2}(z^2+(1-z)^2), \tag{1.66}$$

$$P_{GG}(z) = 6\left[\frac{z}{(1-z)_+} + \frac{1-z}{z} + z(1-z)\right] + \frac{33-2n_f}{6}\delta(1-z). \tag{1.67}$$

In equations (1.64-1.67), the so-called '+' notation is used, which is defined as

$$\int_0^1 \mathrm{d}z \frac{f(z)}{(1-z)_+} = \int_0^1 \mathrm{d}z \frac{f(z)-f(1)}{1-z} = \int_0^1 \mathrm{d}z \ln(1-z)\frac{\mathrm{d}}{\mathrm{d}z}f(z), \tag{1.68}$$

where $f(z)$ is some test function which is regular at the end points.

CHAPTER 2

THE EXPERIMENTAL SET-UP

The Chicago-Columbia-Fermilab-Rochester (CCFR) neutrino experiment was performed in the Fermi National Accelerator laboratory, Fermilab. The CCFR experiment uses a wide-band neutrino-antineutrino beam produced by the Fermilab 800 GeV protons. The CCFR detector which was used to observe neutrino interactions consists of an 690 ton iron based target-calorimeter and a magnetized, muon spectrometer. The experimental data were collected in experiments E744 and E770. E744 ran from February to August of 1985 and E770 ran from June 1987 to February 1988.

In this chapter, the CCFR experiment is outlined. For more detailed descriptions of the experiment consult [8], or [9]. In the first section, creation and the major properties of the neutrino beam used for the experiment is described. The second section is devoted to the CCFR detector while the third section describes the acquisition of the experimental data from the detector.

2.1 Neutrino Beam

The neutrino beam used for the CCFR experiment was created using the 800 GeV Fermilab Tevatron protons. This energy –although Tevatron can achieve energies of 1 TeV– is chosen for optimal machine performance. The path from

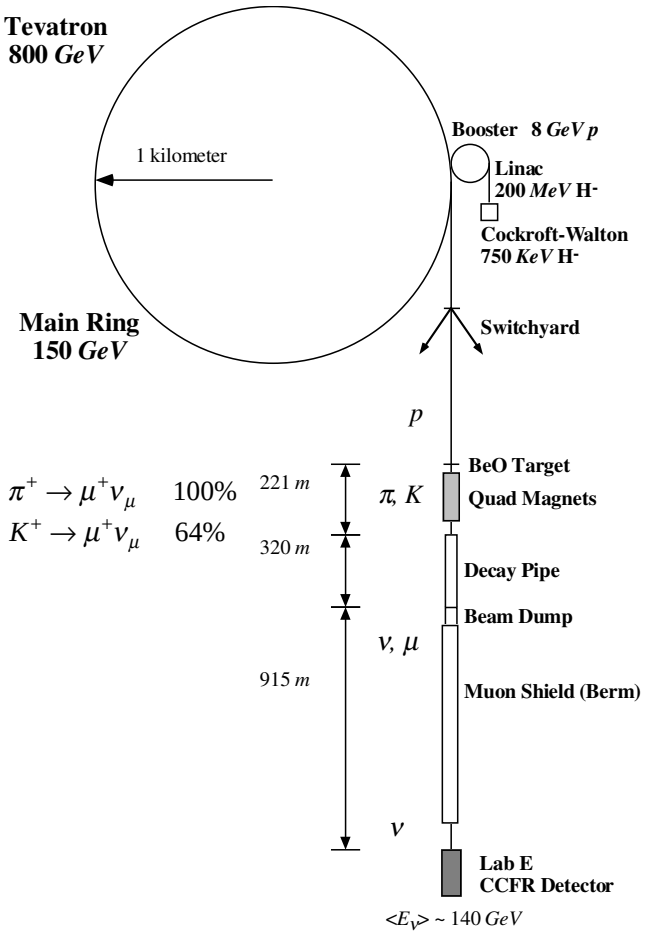

Figure 2.1: The Fermilab neutrino beamline.

high energy protons accelerated at Tevatron to the neutrinos at the CCFR detector is depicted in Fig. 2.1.

Protons are extracted from Tevatron in 1.2 millisecond time intervals, which are called fast spills. In each spill, approximately 10^{12} protons are extracted. These protons are targeted to 33 cm long beryllium-oxide rods. The scattering of accelerated protons and the nuclei of beryllium atoms yields a secondary beam of mesons, which are mostly pions and kaons. Collimated by three quadrupole magnets, the meson beam enters the decay region. In order to obtain a high intensity beam, no sign or momentum selection is made on the meson beam. In

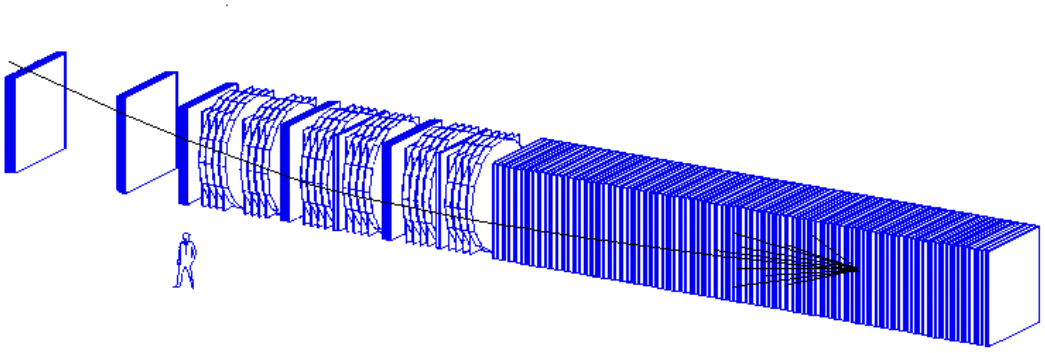

Figure 2.2: The CCFR Detector.

the decay region, mesons decay into tertiary leptons: muons and neutrinos,

$$\pi^+ \rightarrow \mu^+ \nu_\mu \qquad \text{BR} = 99.99\%,$$
$$K^+ \rightarrow \mu^+ \nu_\mu \qquad \text{BR} = 63.5\%$$

where BR are the branching ratios of the specified processes. As the energy of a neutrino which is the product of a meson two-body decay depends on the mass of the parent particle, the neutrino beam has a dichromatic energy spectrum due to the difference between the pion and kaon masses.

All the decay products pass through a long shield of concrete and steel, in which all the particles except neutrinos are absorbed. The result is a mixed beam of neutrinos and antineutrinos having a mean energy of 140 GeV and a maximum energy as high as 600 GeV. With every spill, about 10^9 neutrinos are produced by this process, approximately ten of which undergoes charged-current interactions in the CCFR detector.

2.2 The CCFR Detector

The CCFR detector consists of an unmagnetized iron-scintillator calorimeter, which also serves as a target for the neutrinos, and a solid iron toroidal magnet muon spectrometer, see Fig. 2.2. The calorimeter is used for the hadronic shower energy, event vertex position and the outgoing muon angle measurements, while the toroid spectrometer is used for the outgoing muon momentum measurement.

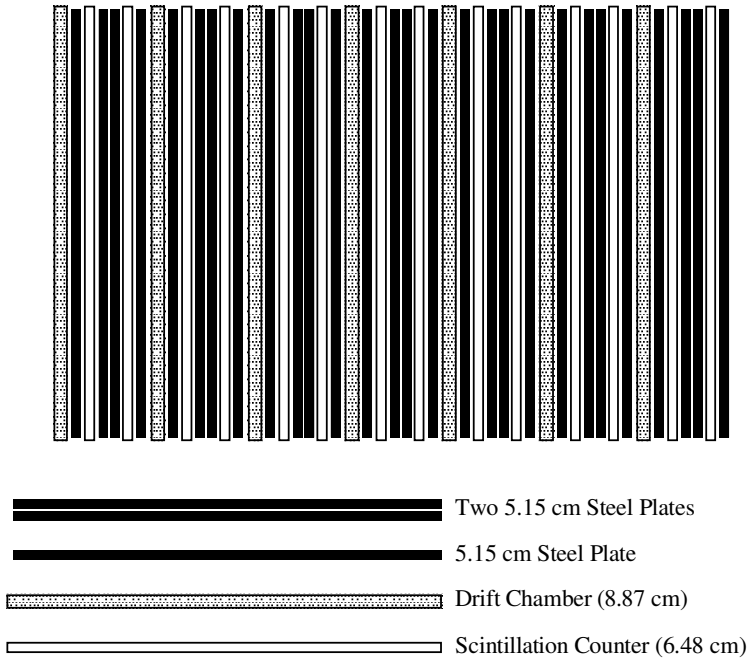

Figure 2.3: Side view of a calorimeter cart.

2.2.1 The target calorimeter

The calorimeter consists of 168 steel plates, 84 liquid scintillation counters and 42 drift chambers, which are installed in the form of 6 identical carts. The calorimeter's transverse dimensions are 10×10 ft^2. Side view of a cart is depicted in Fig. 2.3. The carts are numbered from downstream to upstream direction*.

The scintillation counters are used for hadronic shower energy measurement. They are 1 inch thick and there is one installed for every two steel plates. Scintillation counters consist of acrylic vessels filled with mineral oil, which is doped with organic scintillator fluors. A charged particle passing through the counter excites the scintillating fluors which then emit blue light. The light is transferred to the edges of the counter by total internal reflection. At the edges, blue light is absorbed and re-emitted as green light, and transferred to the four corners by the wave-shifter bars. Finally, the light that reached the edges is collected by four photomultipliers. The electric signals from the phototubes are

* Remembering that a liquid flows from up, to down may help the upstream-downstream terms confused.

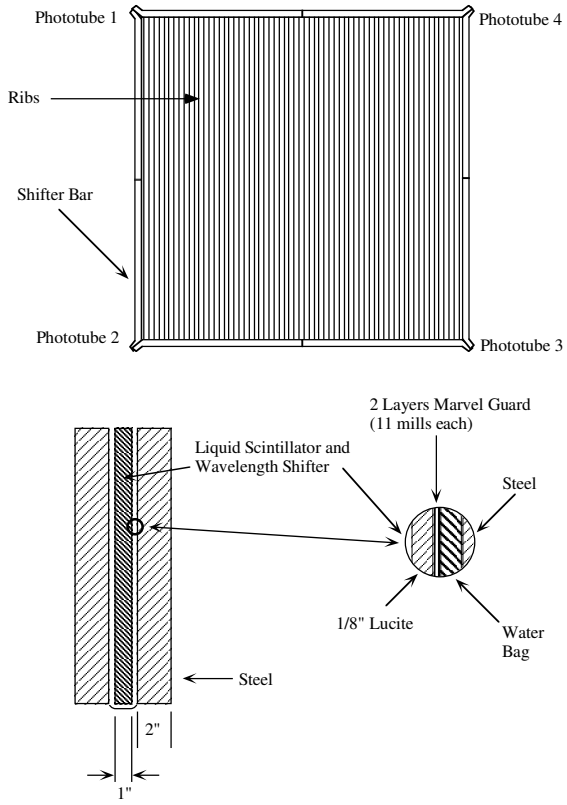

Figure 2.4: Side and transverse view of a scintillation counter.

digitized by analog-digital converters (ADCs).

Drift chamber stations consist of two planes of drift cells, see Fig. 2.5. Each plane has 24 drift cells and the cell orientations of these planes are perpendicular. The cells have a field wire in the middle, and two sense wires closely located at left and right of the field wire. The chambers are filled with an equal mixture of argon and ethane gas. When a charged particle passes through the chamber, it ionizes the gas atoms. The freed electrons drift toward the anode wires and the particle's position is determined from the electrons' drift time. Using two sense wires resolves the left-right ambiguity as the electrons drift toward the closest wire.

The electric signals from the chamber stations are amplified by the pre-amplifier cards located on the chambers, and then sent to two coupled TDCs (Tabular Data Control), which digitizes the time of the signals.

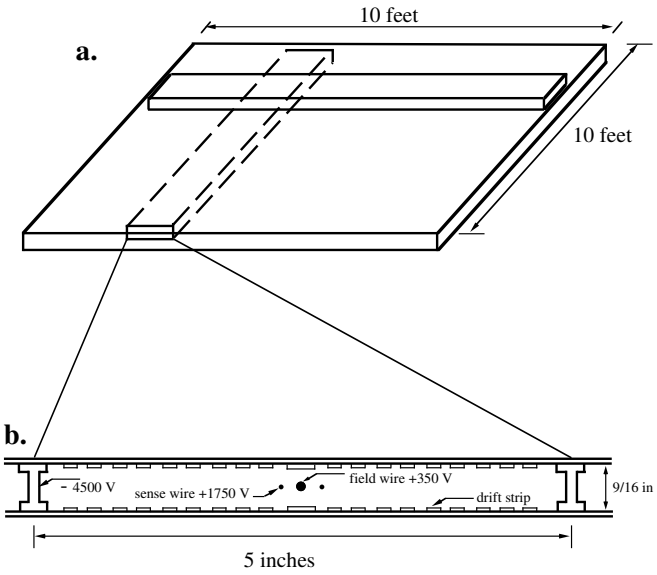

Figure 2.5: A calorimeter drift chamber station.

2.2.2 The muon spectrometer

The muon spectrometer is located downstream of the target calorimeter, which consists of three toroidal iron magnets instrumented with acrylic scintillation counters and three sets of drift chambers, see Fig. 2.6. Each of the three instrumented magnets is referred to as a toroid cart. There are two additional sets of drift chambers at the downstream end of the spectrometer, which are called the blue cart.

Each magnet is constructed from eight cylindrical 8 inch thick washers. The washers have 70 and 5 inch outer and inner radii, respectively. A current of 1200 A creates a magnetic field of about 1.9 Tesla near the center (the washer inner radius) and 1.55 Tesla near the outer edge of the washer. This magnetic field gives a 2.4 GeV transverse momentum component to a muon which travels the length of the spectrometer. Except the proximity of the two iron legs supporting the washers from the below where there is a small radial component, the field is azimuthally uniform.

Positions of the muons penetrating the spectrometer are tracked by the

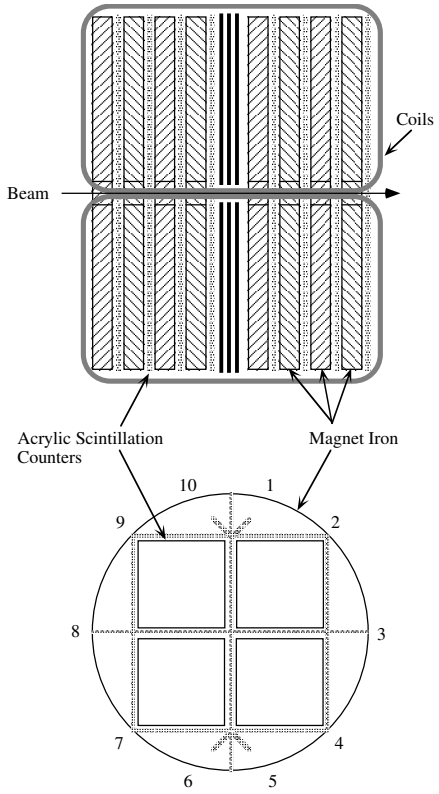

Figure 2.6: Top and transverse views of a CCFR spectrometer cart. In the transverse view, shaded lines indicate the wave shifter bars and numerals indicate the phototube installation locations.

drift chambers. There are a total of five drift chambers, three of them located immediately downstream of each toroid cart, and two (the blue cart) located 3 and 7 meters downstream of the last toroid cart.

2.3 Data Acquisition

The data acquired from the detector consists of electric signals like scintillation counter pulse heights, the drift chamber hits and the timing pulses. This raw data must be converted into physical quantities describing a neutrino interaction, i.e the hadronic energy, the muon angle, etc.

The need of a means of selecting the events of interest among the various

events occurring in the detector, such as CC reactions, neutral current (NC) reactions, and events due to the cosmic ray background is fulfilled by the *triggers*. Triggers initiate the recording of raw detector data, in case certain conditions are satisfied.

The CCFR data acquisition system has six triggers. The first trigger is used to select CC events, while the second is used for NC events. The third trigger is used to study muons ranging out in the calorimeter. The fourth trigger is similar to the first trigger and is used to measure the first trigger's inefficiency. The fifth trigger is the test-beam trigger. The sixth trigger is the straight-through trigger, it selects muons produced upstream of the detector that pass through the entire detector, and is used for calibration and drift-chamber alignment purposes.

After the recording of accepted events on tapes[†], offline processing which involves reconstruction of the events from the raw detector data begins. In this process, first the conversion of raw ADC pulse heights to hadronic energy and of TDC times acquired from drift chambers to hit positions is made. Then a pattern recognition algorithm fits muon tracks to the hit positions, hence determines the muon angle and energy. With the calculation of the kinematic variables x and y, raw detector response information is reduced to the physical information describing the neutrino interactions. The result of the offline processing is recorded in computer environment with the data summary tape (DST) format. The event reconstruction procedure is described in more detail in the next chapter.

[†] The raw data collected in both experiments make approximately 300 GBs of information.

CHAPTER 3

EVENT RECONSTRUCTION AND SIMULATION

3.1 Event Reconstruction

In the laboratory system, a neutrino event is described by three physical quantities: the total hadronic shower energy $E_{\rm had}$, and the energy and zenith angle of the outgoing muon, E_μ and θ_μ. The event reconstruction procedure consists of finding these three quantities which make up an event from the raw detector data.

3.1.1 Hadronic energy measurement

The hadronic final state of the neutrino interaction is a shower of hadrons, most of which are pions. Assuming that the shower is well contained within the fiducial volume of the calorimeter, the energy of the shower is completely absorbed by the calorimeter. The amount of the shower energy is measured by the energy deposited in the scintillators, which is about 3% of the total shower energy. Actually, the ratio of the energy deposited in the scintillators to the total shower energy must be precisely determined for a robust measurement. This is done by the calibration process, yielding the calibration constants which

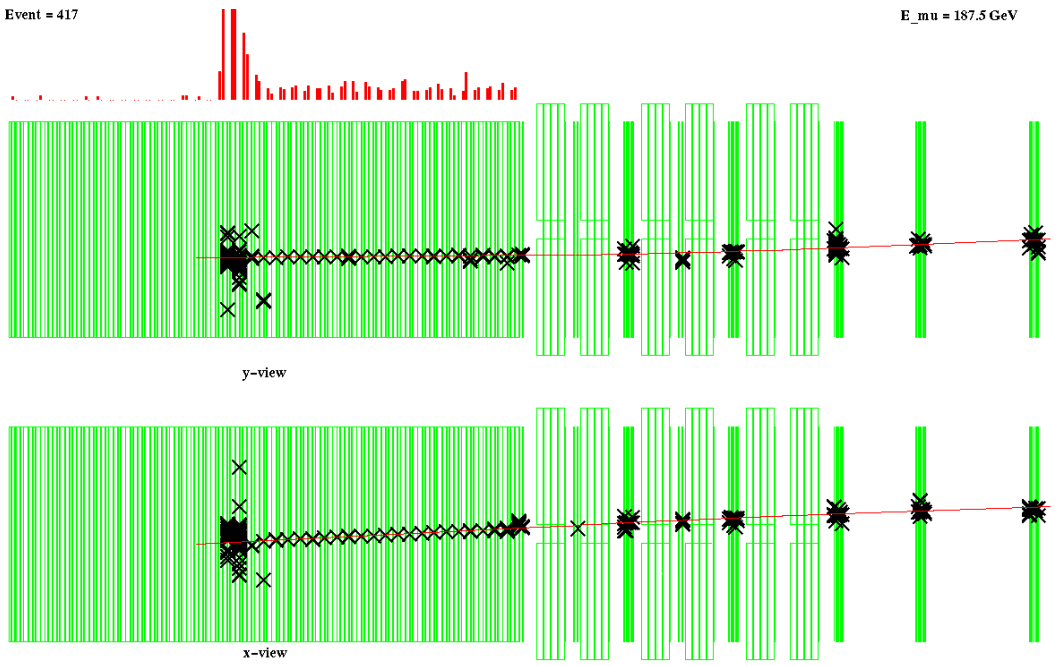

Figure 3.1: A typical reconstructed charged-current event.

correspond to these ratios.

Scintillator (hereafter, *counter*) responses need attention before being accepted, since each of the 84 counters have a slightly different response to the passage of charged particles. Their response may have a dependence on the time, and the location of the charged particle passage. Corrections for these effects are made before calorimeter calibration, which is called the counter gain calibration.

The energy deposited in the counters by a high-energy muon via ionization is almost independent of the muon's energy. Hence, the deposited energy by a 77 GeV muon is taken as a reference value and this energy is said to be deposited by a "minimum ionizing particle", a MIP. This term also refers to the amount of the deposited energy itself.

Using a large sample of straight through test muons, the deposited energies are measured as a function of location from the counter center and as a function of time. The counter response is normalized to the response at the center. The

time variation of a counter's gain is measured using muons passing from the central zone of the counter. As a result, map and gain corrections are applied to the data such that all counters yield the same response for a MIP, as a function of position and time.

For the calorimeter calibration, electron, muon and hadronic test beams are used. The hadronic test beam consist mainly of pions. The calibration runs took place before the experiment E744, and after the experiment E770. To perform the calibration, first the entire calorimeter is taken out of the test beam, then each calorimeter cart is exposed to the test beam individually. Hence each cart has it's own calibration, yet they are all found to be the same as expected. The calibration is made by comparing the calorimeter response, with the known energy of the test beam. With the test beam, also the calorimeter resolution σ is measured.

In order to measure the shower energy, the shower region must be determined first. The beginning of a shower is the most upstream counter for which the energy deposition in two consecutive counters is more than 4 MIPs of energy, and is referred as the PLACE. The end of the shower, so called SHEND, is the counter the energy deposition of whose three consecutive counters is less than 4 MIPs. The shower is said to be enclosed in the region of counters from PLACE to SHEND-5^*, and the shower energy is the sum of the individual energies of the counters in this region. The mean energy response of the calorimeter $< E/p >$ for a hadronic test beam of momentum p is found to be 4.74 MIPs/GeV.

3.1.2 Muon angle and energy measurement

Muon tracks are determined by a fitting algorithm which uses the hit data from the drift chambers. The muon track in the calorimeter is almost a straight line and is used to determine the muon production angle. The bending of the muon track in the toroid is used for the muon momentum determination. Both measurements are complicated by multiple Coulomb scattering (MCS) effects.

* Note that the counters are numbered from downstream to upstream direction.

As the amount of multiple scattering depends on the muon momentum, MCS introduces a correlation between muon momentum and muon angle measurements. Due to this correlation, the measurement of muon angle is iterated again using the final measurement of muon momentum.

While calculating the muon angle, the drift chamber hits near PLACE are omitted from the fit because in this region there are extra hits produced by the shower particles. As the hadronic energy increases, more hits are omitted. As the MCS effect is proportional to the muon momentum, the uncertainty in the measurement of muon angle depends on both the muon momentum and the energy of the hadronic shower.

The angular resolution of the detector is found by using a sample straight-through muons, and the muon momentum resolution is obtained from a test beam of 120 GeV muons.

Muons entering the CCFR detector loses one GeV of energy for every three drift chamber they penetrate. The total muon energy E_μ is found by adding the energy losses in the target, both inside and outside of the shower region, to the energy at the front face of the toroid. The muon energy at the shower region cannot be determined directly; it's calculated by a certain parameterization, which gives the mean energy loss per counter as 0.1595 GeV. The energy loss outside the shower region is found by summing the energy depositions in the counters which are in this region.

3.1.3 Event selection

In order to increase the quality of the event data, cuts are applied to the reconstructed events. Among these cuts are the fiducial volume cuts, which are applied to make sure that the events are occurred at a time period during which the beam and the detector are fully operational and to ensure that the interaction took place in a geometrical region where the detector response is robust, geometric cuts, applied to ensure a good muon momentum measurement from

the spectrometer response, dimuon cut, to eliminate dimuon events whose acceptance might significantly affect xF_3 measurements in the low x-range, and the total cross-section cuts, applied to assure in the cross-section measurement that the muons are well measured.

3.2 The Monte-Carlo Simulation

The measured event data do not reflect exactly what really happened in the detector due to the effects of detector geometry, detector resolution, kinematic cuts, and various physics effects such as the mass of the charm quark. To get the true number of charged-current events occurred in the detector which will be used for the differential cross-section and structure function extraction, the event sample must be corrected for these detector resolution and acceptance effects. This correction is made by using an event sample generated by a Monte-Carlo (MC) simulation program, which is called the Fast Monte-Carlo.

The simulation first generates CC neutrino events according to a given beam flux and differential cross-section model, then mimics the reconstruction procedure, applying the experimental effects such as acceptance and resolution smearing. Since the beam flux and the differential cross-sections are not *a priori* known, an iterative approach is used. First MC is run with an initial model for the flux and differential cross-sections. Then using the corrections obtained from the simulation, flux and differential cross-sections are extracted from the experimental data. After this, MC is re-run with these results. This procedure is repeated until the results of MC and the experimental measurement converge.

3.2.1 Event generation

Generation of an event consists of generation of a number of physical quantities describing an event. Generated values and the way they are generated are as following:

1. Randomly select the incoming particle type, neutrino or an antineutrino,

and select the polarity of the toroid. Here, the final ratio of the number of antineutrino events to the neutrino events is normalized to the data.

2. Randomly generate the neutrino energy, according to the provided flux distribution $\Phi(E)$. Using the flux distribution measured from the data, randomly generate the transverse vertex position in the $x-y$ plane (downstream direction describes the z axis).

3. According to the differential cross-section model, randomly generate the kinematic variables x and y. Using these values and the generated neutrino energy, calculate the hadronic energy, muon energy at the interaction vertex and the muon zenith angle θ_μ. The azimuth angle ϕ_μ of the muon is generated uniformly between 0 and 2π.

4. Randomly generate PLACE, the z-location of the interaction vertex in the calorimeter. Using a shower length distribution determined from the data, randomly generate the shower length.

5. Propagate the muon track through the calorimeter. The energy loss of muons, whose interaction vertex energies are less than 5 GeV is due to ionization losses (restricted energy loss) and is simulated according to range-energy tables. Simulation of energy losses of muons with energy greater than 5 GeV include ionization and the catastrophic energy loss sources of bremsstrahlung, pair production and δ-ray production.

6. When the muon track reaches the front face of the spectrometer, muon energy at this location is found by subtracting the total energy loss of the muon from it's energy at the interaction vertex.

For a charged-current event, the neutrino energy, hadronic energy, muon vertex energy, muon zenith and azimuth angles, restricted and catastrophic muon energy losses and the muon energy at the front face of the spectrometer are smeared by the MC to simulate detector resolution effects.

3.2.2 The differential cross-section model

The MC simulation depends on a model of the physical cross-sections in terms of the parton distribution functions (PDFs). In the model, the differential cross-section is expressed in the usual form:

$$\frac{1}{E_\nu}\frac{\mathrm{d}^2\sigma^{\nu(\bar{\nu})}}{\mathrm{d}x\,\mathrm{d}y} = \frac{G_F^2 M_N}{\pi}\left[\frac{1}{2}y^2\cdot 2xF_1 + \left(1-y-\frac{M_N x y}{2E_\nu}\right)F_2 \pm \left(y-\frac{1}{2}y^2\right)xF_3\right]. \tag{3.1}$$

In leading order, the structure functions are parameterized directly in terms of parton density functions:

$$\begin{aligned} 2xF_1(x,Q^2) = \big[&xu_v(x,Q^2) + xd_v(x,Q^2) + \\ &2xu_s(x,Q^2) + 2xd_s(x,Q^2) + 2xs_s(x,Q^2)\big], \end{aligned} \tag{3.2}$$

$$F_2(x,Q^2) = 2xF_1(x,Q^2)\times\frac{1+R(x,Q^2)}{1+4M^2x^2/Q^2}, \tag{3.3}$$

$$xF_3(x,Q^2) = xu_v(x,Q^2) + xd_v(x,Q^2). \tag{3.4}$$

Here the contribution of the charm sea is assumed to be zero, and R is the ratio of the longitudinal and transverse cross-sections, see eq. (1.51). In the cross-section calculation, the parton distribution function set suggested by Buras and Gaemers (BG) was used [10]. BG model uses 13 parameters to describe the parton distributions and is equivalent to a leading order QCD model, however it does not depend on any specific QCD assumptions. The fit parameters are determined by iteratively fitting the model to the experimental data.

BG parton distributions receive two corrections before being fitted to the differential cross-sections. One is the d/u correction, which is applied since the CCFR detector has a small non-isoscalarity. The other is the low Q^2 correction, applied since the BG PDFs are not reliable for $Q^2 < 1$ GeV^2. This correction involves the use of GRV94 PDFs [11], since these PDFs are dynamically generated. First the GRV94 PDFs are normalized to BG PDFs at $Q^2 = 1.35$ GeV^2, then by using their Q^2 evolution, BG PDFs are extended down to $Q^2 = 0.23$ GeV^2.

The cross-section model described above is fitted to the CCFR cross-section

data iteratively, yielding a chisquare-degree of freedom ratio of $\chi^2/\mathrm{DOF} = 2676/2750$.

As the BG PDFs are found by fits to the CCFR differential cross-section data, some of the non-perturbative effects such as the higher twist and target mass effects are already included in the PDFs. However, since there is no differential cross-section data in the low Q^2 and high x region, there are unaccounted higher twist effects. The higher twist effects are extracted from the SLAC and BCDMS F_2 data and introduced to the BG prediction by adding a $ht(x)/Q^2$ correction term to $F_2(\mathrm{LO})$ as following:

$$F_2(x, Q^2) = F_2(\mathrm{LO}) \left(1 + \frac{ht(x)}{Q^2}\right) \tag{3.5}$$

where

$$ht(x) = \begin{cases} \mathrm{Max}\left[0.672\left(\frac{x^{1.893}}{1-1.138x} - 0.256\right), 5.0\right] & x > 0.4 \\ 0 & x < 0.4 \end{cases} \tag{3.6}$$

Since in the high x region F_2 and xF_3 are expected to have a similar behavior, the same higher twist correction is applied to the BG xF_3 prediction.

In the leading order, the ratio of the longitudinal cross-section and the transverse cross-section R vanishes. However, perturbative and non-perturbative QCD effects assign R a finite value. To calculate R, the following empirical parameterization to the world's available data is used [12]:

$$R_{\mathrm{World}}(x, Q^2) = \frac{0.0635}{\ln(Q^2/0.04)}\theta + \frac{0.5747}{Q^2} - \frac{0.3534}{Q^4 + 0.09}, \tag{3.7}$$

where

$$\theta = 1 + \frac{12\,Q^2}{Q^2 + 1} \times \frac{(0.125)^2}{(0.125)^2 + x^2}, \tag{3.8}$$

which is known to be a good parameterization in the intervals $0.07 < x < 0.7$ and $1.0 < Q^2 < 75$ GeV^2.

For the case of a produced charm quark in the final state, the Björken variable x no longer represents the momentum fraction carried by the struck

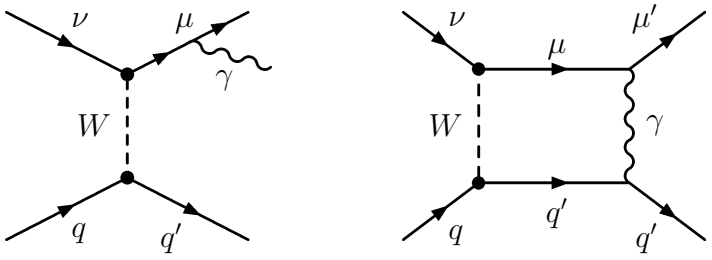

Figure 3.2: Electroweak radiative processes included in the Bardin's calculation.

quark in the Breit frame. This is due to the fact that the charm quark's mass is far from being zero: $m_c \simeq 1.3$ GeV. So, x variable must be replaced by the slow rescaling variable $\xi = (1 + m_c^2/Q^2)x$ to introduce charm production to calculations. In other words, the x arguments of structure functions need to be transformed to ξ variables. Structure functions whose argument are x variable now that are called the non-charm production component and the ones with argument ξ are called the charm production component. Resultant structure functions are found by adding these two components.

Corrections to account for the radiative effects are introduced according to the Bardin's calculation [13]. Bardin's calculation includes the effect of photon emission from the outgoing muon and the effect of photon exchange between the outgoing muon and the struck quark –see Fig. 3.2.

CHAPTER 4

CROSS-SECTION MEASUREMENT AND STRUCTURE FUNCTION EXTRACTION

4.1 Differential Cross-Section Measurement

In this section, CCFR inclusive charged-current (anti)neutrino-nucleon scattering differential cross-section measurement is outlined.

The differential cross-sections $\mathrm{d}^2\sigma^{\nu,\bar{\nu}}/E\mathrm{d}x\mathrm{d}y$ are measured as functions of E, x and y. The extraction is performed using the following expression:

$$\frac{1}{E}\frac{\mathrm{d}^2\sigma}{\mathrm{d}x\,\mathrm{d}y}(<E>,<x>,<y>) = \frac{N(E,x,y)\frac{MC^{\mathrm{gen}}(<E>,<x>,<y>)}{MC^{\mathrm{smr}}(E,x,y)}}{k\phi(<E>)<E>\Delta x\Delta y}, \qquad (4.1)$$

where $N(E,x,y)$ is the number events in a particular E, x and y bin. MC^{gen} and MC^{smr} are the number of Monte-Carlo events before and after the inclusion of the detector resolution smearing effects and differential cross-section event selection cuts, hence the ratio of MC^{gen} and MC^{smr} corresponds to the acceptance correction, which also includes detector resolution effects. The variables $<E>$, $<x>$ and $<y>$ correspond to the average values of these quantities in each bin. In the above equation, Δx and Δy corresponds to the bin widths of x and y bins, and ϕ is the measured relative flux, which is normalized by the factor k for the CCFR detector.

4.1.1 Beam flux measurement

The neutrino flux is extracted by the fixed-ν method, where, $\nu = E_{\rm had}$. The fixed-ν method uses a subset of the CC events; a sample with low hadronic energy. This method cannot provide the overall absolute normalization of the flux, however it reliably provides the energy dependence of the flux and the ratio of neutrino and antineutrino fluxes as a function of energy. That's why, this method is also called the relative flux method.

Fixed-ν method is derived from the formalism of CC neutrino-nucleon cross-section and gives the flux via the following expression:

$$N(E_\nu)_{\nu<\nu_0} = \phi(E_\nu) \int_0^{\nu_0} {\rm d}\nu\, A \left[1 + \frac{\nu}{E}\left(\frac{B}{A}\right) - \frac{\nu^2}{2E^2}\left(\frac{B}{A} - \frac{\int F_2 \tilde{R}}{\int F_2}\right)\right], \quad (4.2)$$

where

$$\frac{B}{A} = -\left[1 \mp \frac{\int_0^1 {\rm d}x\, x F_3(x,Q^2)}{\int_0^1 {\rm d}x\, F_2(x,Q^2)}\right], \quad (4.3)$$

and

$$\tilde{R} = \quad \frac{\nu + 2M_N x}{(1+R)\nu} - \frac{M_N x}{\nu} - 1. \quad (4.4)$$

Here, $-(+)$ corresponds to neutrino (antineutrino) interactions.

The data sample used for the flux extraction is the subset of the events which pass the standard CC analysis cuts, with $E_{\rm had} < \nu_0 = 20$ GeV. This limit both has sufficient data from higher energy bins, and also is low enough to minimize the correlation with the differential cross-section data sample, which includes all the data for $E_{\rm had} > 10$ GeV. The number of events that pass the flux analysis cuts is $390,000$ for neutrino and $86,000$ for the antineutrino case. The relative flux is found from (4.2) as:

$$\phi(E_\nu) \propto \frac{N(E_\nu)_{\nu<\nu_0}}{\int_0^{\nu_0} {\rm d}\nu\, A \left[1 + \frac{\nu}{E}(<B/A>) - \frac{\nu^2}{2E^2}\left((<B/A>) - \frac{\int F_2 \tilde{R}}{\int F_2}\right)\right]}, \quad (4.5)$$

where $<B/A>$ is the average of the B/A values over all energy bins. Here, raw event data $N(E_\nu)_{\nu<\nu_0}$ is corrected for detector acceptance and resolution

smearing effects before the flux extraction. The value of $\int F_2\tilde{R} / \int F_2$ is calculated using the BG differential cross-section model described in the previous chapter. The B/A values for each E_ν bin is determined by dividing the bins to eight 2 GeV wide $E_{\rm had}$ bins, then fitting to the N_ν distribution in each energy bin. It was seen that the extracted B/A values are almost independent of the energy, hence the values which are averaged over all energy bins are used.

The MC corrections applied to the event data for detector acceptance and resolution smearing effects are sensitive to the functional form of the differential cross-sections. Hence, the flux and differential cross-section extractions are performed iteratively, until they converge.

In order of importance, the systematic errors in the relative flux extraction are as following:

- The uncertainties in the value of $< B/A >^{\nu,\bar{\nu}}$, which is the largest dominant systematic error source. This effect is very large at low energies.

- The calibration error in the measurement of E_μ. The measurement of the neutrino energy for the low $E_{\rm had}$ flux events mainly originates from the muon energy, hence any mis-measurement of E_μ results in changing the extracted flux. A typical effect for 1% mis-calibration of E_μ is less than 5% for neutrinos and 10% for antineutrinos.

- The error in the $E_{\rm had}$ calibration. In fact this effect is weak since the relative flux is insensitive to the calibration, as it is a 'relative' flux.

The absolute normalization factor is obtained by normalizing the relative flux to the average of the world neutrino-nucleon cross-section data for isoscalar iron target. Measured average cross-section of the CCFR collaboration using the relative flux in the 30 to 200 GeV range was normalized to the world average value of the neutrino cross-section $\sigma^\nu/E = 0.677 \times 10^{-38}$ cm^2/GeV per nucleon. This value was used in the following relation:

$$\sum_{30}^{200} N(E_i) \frac{MC(E_i)_{\rm gen}}{MC(E_i)_{\rm smr}} = k \frac{\sigma_{\rm world,iso}}{E} \sum_{30}^{200} \phi(E_i) E_i \times \left[\frac{\sum_{30}^{200} \frac{\sigma_{\rm world,fe}}{E} \phi(E_i) E_i}{\sum_{30}^{200} \frac{\sigma_{\rm world,iso}}{E} \phi(E_i) E_i} \right] \quad (4.6)$$

Here, left hand side is the MC-corrected total number of events from 30 to 200 GeV. The first factor on the right hand side is the total number of events for an isoscalar target using the world average total cross-section, while the second factor is a non-isoscalarity correction for the iron target, which is equal to the ratio of the number of Monte-Carlo events from an isoscalar target to the events from a non-isoscalar iron target. The overall uncertainty in the normalization is about 2%, which originates from the uncertainty in the average value of the all world total cross-section measurements.

4.1.2 Differential cross-section extraction

The data sample used for differential cross-section extraction is found by applying the following cuts to the event data (the intervals represent accepted events):

- $E_{had} > 10$ GeV cut, to minimize the correlation between the flux and the structure function data samples, since event data with low hadron energy ($10 < E_{had} < 20$ GeV) are used for neutrino flux determination.
- $Q^2 > 0.3$ GeV^2, since very low Q^2 events are not well modelled in the differential cross-section model of the Monte-Carlo simulation.
- $30 < E_\nu < 360$ GeV, to ensure a reasonable set of both flux and structure function data. The lower limit excludes the region with large acceptance corrections, and the upper limit excludes the region where the Monte-Carlo smearing corrections have an high error.

The E_ν, x and y bins are chosen according to the population of events, and also to match the subsequent structure function bins. In order to eliminate non-physical kinematic region which is due to the outgoing muon having non-zero mass is also considered in the selection of the x and y bins.

The differential cross-sections are extracted using eq. (4.1) for the experiments E774 and E770, separately. Thereafter, two sets of cross-sections are combined together with their statistical and systematical errors.

4.2 Structure Function Measurement

4.2.1 Methodology

Nucleon structure functions F_2 and xF_3 are measured from neutrino-nucleon scattering by using the observed number of neutrino and antineutrino events:

$$N^{\nu,\bar{\nu}}(x,Q^2) = \int_{\text{x-bin}} \mathrm{d}x \int_{Q^2\text{-bin}} \mathrm{d}Q^2 \int_{\text{all energies}} \mathrm{d}E \, \frac{\mathrm{d}\sigma^{\nu,\bar{\nu}}}{\mathrm{d}x \, \mathrm{d}Q^2} \Phi^{\nu,\bar{\nu}}(E), \tag{4.7}$$

here, the x and Q^2 integrations are over the bin limits, while the energy integral runs over the entire energy spectrum in the range of the flux. The x and Q^2 binning of the data can be found in Table 4.1. The differential cross-section can be replaced with the general expression in terms of the structure functions:

$$\frac{\mathrm{d}\sigma^{\nu,\bar{\nu}}}{\mathrm{d}x \, \mathrm{d}Q^2} = \frac{G^2}{2\pi x} \left[\left(1 - y - \frac{M_N x y}{2E} \right) F_2 + \frac{y^2}{2} 2xF_1 \pm y \left(1 - \frac{y}{2} \right) xF_3 \right], \tag{4.8}$$

where +(-) terms correspond to neutrinos (antineutrinos). The structure function $2xF_1$ can be removed from this expression using

$$2xF_1 = F_2 \frac{1 + 4M_N^2 x^2/Q^2}{1+R}, \tag{4.9}$$

where $R = \sigma_L/\sigma_T$. The parameterization of R used in the CCFR structure function measurement is found from the world's available data on the measurement of R, see eq. (3.7). Substituting equations (4.8) and (4.9) into (4.7) we get,

$$\begin{aligned} N^{\nu,\bar{\nu}}(x,Q^2) = {} & \frac{G^2 M}{\pi} \int \mathrm{d}x \int \frac{\mathrm{d}Q^2}{2MEx} \int \mathrm{d}E \, E \Phi^{\nu,\bar{\nu}}(E) \times \\ & \left[\left(1 - y - \frac{Mxy}{2E_\nu} + \frac{y^2}{2} \frac{1 + 4M^2x^2/Q^2}{1 + R(x,Q^2)} \right) F_2(x,Q^2) \pm y \left(1 - \frac{y}{2} \right) xF_3(x,Q^2) \right]. \end{aligned} \tag{4.10}$$

As the x and Q^2 bins are small, the structure functions do not vary significantly within each bin, hence they may be taken outside of the integral. For each x and Q^2 bin, eq. (4.10) gives a system of two linear equations whose two unknowns

are the two structure functions in this particular bin:

$$\begin{aligned} N^{\nu}(x,Q^2) &= A^{\nu}\, F_2(x,Q^2) + B^{\nu}\, xF_3(x,Q^2), \\ N^{\bar{\nu}}(x,Q^2) &= A^{\bar{\nu}}\, F_2(x,Q^2) - B^{\bar{\nu}}\, xF_3(x,Q^2), \end{aligned} \tag{4.11}$$

where

$$\begin{aligned} A^{\nu,\bar{\nu}} = \frac{G^2 M}{\pi} \int\int\int \mathrm{d}x\, \frac{\mathrm{d}Q^2}{2MEx}\, \mathrm{d}E\, E\Phi^{\nu,\bar{\nu}}(E) \times \\ \left(1 - y - \frac{Mxy}{2E_\nu} + \frac{y^2}{2}\frac{1 + 4M^2x^2/Q^2}{1 + R(x,Q^2)}\right), \end{aligned} \tag{4.12}$$

$$B^{\nu,\bar{\nu}} = \frac{G^2 M}{\pi} \int\int\int \mathrm{d}x\, \frac{\mathrm{d}Q^2}{2MEx}\, \mathrm{d}E\, E\Phi^{\nu,\bar{\nu}}(E) \left(y - \frac{y^2}{2}\right), \tag{4.13}$$

and

$$xF_3 = < xF_3^{\nu,\bar{\nu}} > = \frac{xF_3^{\nu} + xF_3^{\bar{\nu}}}{2}. \tag{4.14}$$

Hence, by solving equations (4.11), and using the experimentally measured number of events $N^{\nu,\bar{\nu}}$, the structure functions are found as:

$$\begin{aligned} F_2(x,Q^2) &= \left(B^{\bar{\nu}} N^{\nu} + B^{\nu} N^{\bar{\nu}}\right) / \det, \\ xF_3(x,Q^2) &= \left(A^{\bar{\nu}} N^{\nu} + A^{\nu} N^{\bar{\nu}}\right) / \det, \\ \det &= A^{\nu} B^{\bar{\nu}} + B^{\nu} A^{\bar{\nu}}. \end{aligned} \tag{4.15}$$

The structure function measurement results of the CCFR experiment can be found in Figures 5.1 and 5.2, along with the QCD fit results.

4.2.2 Systematic effects

Systematic uncertainties considered in the structure function extraction are as following:

The experimental systematics:

- Hadron energy calibration (C_{HAD}^{744}, C_{HAD}^{770}): Due to the aging of the scintillator oil in the target counters, the readjustment of the PMT voltages and the changes made in the read-out electronics, the hadron energy calibration is known to within 1%. Hence the calibration of each of the two experiments E744 and E770 is allowed to be independently shifted by $\pm 1\%$.

Table 4.1: x and Q^2 binning of the CCFR structure function data.

#	x-bins	Q^2-bins
1	0.0075	1.3
2	0.0125	2.0
3	0.0175	3.2
4	0.025	5.0
5	0.035	7.9
6	0.05	12.6
7	0.07	20.0
8	0.09	31.6
9	0.11	50.1
10	0.14	79.4
11	0.18	125.9
12	0.225	199.5
13	0.275	
14	0.35	
15	0.45	
16	0.55	
17	0.65	
18	0.75	

- $E_{\rm had}$ shift (ΔE_{HAD}): The data is corrected for a disagreement in the model of the hadron energy in the Monte-Carlo and the event data. The error in this correction is estimated to be $\pm$100 MeV.

- Muon energy calibration (C_μ): This error is due to the muon energy being known within $\pm 1\%$.

- E_μ shift (ΔE_μ): This error is introduced to provide the systematic error for E_μ in consistence with the $E_{\rm had}$ calibration systematic error calculation model. The error is assumed to be $\Delta E_\mu \pm 100$ MeV.

The flux-extraction systematics:

- B/A for neutrinos and antineutrinos $[(B/A)^{\nu,\bar{\nu}}_{E744,E770}]$: This error is due to the uncertainty in the value of B/A, which affects the flux. The systematical errors due to this uncertainty are calculated separately for the E744 and E770 experiments, for ν and $\bar{\nu}$ cases.

- Flux adjustment (Φ^{adjusted}): An adjustment was made to the measured beam flux to account for a small non-linear behavior of the measured partonic level cross-sections. The flux being adjusted and not adjusted is treated as a systematic error. Note that this error has no '$-\delta$' shift.

The Cross-section systematics:

- Cross-section normalization (σ^{ν}/E): This uncertainty is due to an error of 2.1% in the world average of the neutrino-iron cross-sections.

- Cross-section ratio ($\sigma^{\bar{\nu}}/\sigma^{\nu}$): This uncertainty is due to an error in the world average of the $\sigma^{\bar{\nu}}/\sigma^{\nu}$ ratio.

The model systematics:

- R_{World} error (δR): The error of the R parameterization used in the analysis is quoted to be $\pm 15\%$ [12].

- Charm quark mass (m_c): Due to the error in the charm quark mass, where $m_c = 1.31 \pm 0.24$ [14].

- Strange sea shape (α), strange sea normalization (κ): These parameters are used in a correction made to the cross-section model to account for the strange sea in the xF_3 extraction procedure. Values and their corresponding errors of these parameters are $\alpha = 2.50 \pm 0.65$ and $\kappa = 0.373 \pm 0.046$ [14].

- Charm branching ratio (B_c): Charm branching ratio enters the calculation via the dimuon correction applied to the cross-section model of the Monte-Carlo. The value of the charm branching ratio is $B_c = 0.105 \pm 0.007$ [14].

- Model Parameterization: This error is due to the choice of the functional form of the physics model used in the Monte-Carlo.

CHAPTER 5

MEASUREMENTS OF $\Lambda_{\mathbf{LO}}$

5.1 The Computer Program

The computer program performing the QCD parameter Λ measurement is written in the `FORTRAN` language on a `RedHat Linux 7.3` system. The measurement is performed by fitting the LO-QCD predictions to the CCFR structure function data [8],[15]. The program consists of the LO-QCD model and the fitting, plotting, reporting machinery, which make approximately 3500 lines of code. Besides displaying the run results on the terminal screen, the program also generates a run report in the LaTeX format.

5.1.1 The QCD model

QCD model provides the QCD predictions of the structure functions F_2 and xF_3 according to the given values of the fit parameters. F_i (F_2 and xF_3) are expressed in terms of the corresponding singlet and nonsinglet quark distributions, as in the leading-order, the relations $F_2 = xq^S$ and $xF_3 = xq^{NS}$ hold. The Q^2 dependencies of the quark distributions are calculated by direct integration of the AP evolution equations (1.57-1.56) in the x space. Finally, the calculated structure functions are corrected to account for the target mass effect.

5.1.1.1 Evolution equations

The evolution of the parton distributions to an arbitrary Q^2 scale is made by directly integrating the AP evolution equations. For convenience, the program performs the evolution using the s variable* instead of the Q^2 variable:

$$s = \ln\left(\frac{t}{t_0}\right), \tag{5.1}$$

where,

$$t = \ln\left(\frac{Q^2}{\Lambda^2}\right), \quad t_0 = \ln\left(\frac{Q_0^2}{\Lambda^2}\right). \tag{5.2}$$

The AP equations (1.57-1.56) are transformed according to the new variable definition as following:

$$\frac{\mathrm{d}q^{NS}(x,s)}{\mathrm{d}s} = t\frac{\alpha_s(t)}{2\pi}\int_x^1 \frac{\mathrm{d}y}{y} q^{NS}(y,s)P_{qq}(x/y), \tag{5.3}$$

$$\frac{\mathrm{d}q^{S}(x,s)}{\mathrm{d}s} = t\frac{\alpha_s(t)}{2\pi}\int_x^1 \frac{\mathrm{d}y}{y}\big[q^{S}(y,s)P_{qq}(x/y) + G(y,s)P_{qG}(x/y)\big], \tag{5.4}$$

$$\frac{\mathrm{d}G(x,s)}{\mathrm{d}s} = t\frac{\alpha_s(t)}{2\pi}\int_x^1 \frac{\mathrm{d}y}{y}\big[q^{S}(y,s)P_{Gq}(x/y) + G(y,s)P_{GG}(x/y)\big]. \tag{5.5}$$

By using the definition (1.68) with the splitting functions (1.64-1.67), the AP integrals (5.3-5.5) can be evaluated. The resultant form of the AP equations that are used by the QCD model of the fitting program are as follows:

$$\begin{aligned}\frac{\mathrm{d}[xq^{NS}(x,s)]}{\mathrm{d}s} =& t\frac{\alpha_s(s)}{2\pi}C_2(F)\Bigg\{\Big[\frac{3}{2} + 2\ln(1-x)\Big]xq^{NS}(x,s) + \\ & \int_x^1 \frac{\mathrm{d}z}{1-z}\Big[(1+z^2)(\frac{x}{z})q^{NS}(\frac{x}{z},s) - 2xq^{NS}(x,s)\Big]\Bigg\},\end{aligned} \tag{5.6}$$

$$\begin{aligned}\frac{\mathrm{d}[xq^{S}(x,s)]}{\mathrm{d}s} =& t\frac{\alpha_s(s)}{2\pi}\Bigg[C_2(F)\Bigg\{\Big[\frac{3}{2} + 2\ln(1-x)\Big]xq^{S}(x,s) + \\ & \int_x^1 \frac{\mathrm{d}z}{1-z}\Big[(1+z^2)(\frac{x}{z})q^{S}(\frac{x}{z},s) - 2xq^{S}(x,s)\Big]\Bigg\} + \\ & n_f T_2(F)\int_x^1 \mathrm{d}z(\frac{x}{z})G(\frac{x}{z},s)[z^2 + (1-z)^2]\Bigg],\end{aligned} \tag{5.7}$$

* Note that $s = 0$ for $Q^2 = Q_0^2$.

$$\frac{\mathrm{d}[xG(x,s)]}{\mathrm{d}s} = t\frac{\alpha_s(s)}{2\pi}\Bigg\{C_2(F)\int_x^1 \mathrm{d}z(\frac{x}{z})q^S(\frac{x}{z},s)\frac{1+(1-z)^2}{z}+ \\ 2C_2(A)\Bigg[\int_x^0 \mathrm{d}z\Bigg\{\frac{z\big[(\frac{x}{z})G(\frac{x}{z},s)\big]-xG(x,s)}{1-z}+ \\ \Big(\frac{x}{z}\Big)G\left(\frac{x}{z},s\right)\left[\frac{(1-z)(1+z^2)}{z}\right]\Bigg\}\Bigg]+\frac{1}{2}\beta_0 xG(x,Q^2)\Bigg\}, \tag{5.8}$$

here the number of quark flavors is taken $n_f = 4$, $C_2(F) = \frac{4}{3}$, $C_2(A) = 3$, $T_2(F) = \frac{1}{2}$ and $\beta_0 = 11 - 2/3\, n_f$.

5.1.1.2 Initial parton distributions and evolution of structure functions

The program starts evolution of the structure functions from a reference value of Q^2, $Q_0^2 = 5$ GeV^2. This value is determined by the target mass correction validity considerations. The singlet and nonsinglet parton distributions q^{NS} and q^S, and the gluon distribution G are initialized for $Q^2 = Q_0^2$ by the following parameterizations:

$$xq^{NS}(x,Q_0^2) = A_{NS}\, x^{\eta_1}(1-x)^{\eta_2}, \tag{5.9}$$

$$xq^S(x,Q_0^2) = A_S(1-x)^{\eta_S} + xq^{NS}(x,Q_0^2), \tag{5.10}$$

$$xG(x,Q_0^2) = A_G(1-x)^{\eta_G}, \tag{5.11}$$

where A_{NS}, η_1, η_2, A_S, η_s, A_G, and η_G are the fit parameters, hence this is the point where the fit parameters other then Λ are introduced into the calculation. These parameterizations are suggested by the expected behavior of the nonsinglet, singlet and the gluon distributions in the $x \to 0$ and $x \to 1$ limits.

Evolution of the structure functions from the reference scale Q_0^2 to an arbitrary scale Q^2 is performed as follows:

1. Integrate the right hand side of the relevant AP equation for the 'current' values of the parton distributions. Note that if $s = 0$, the values from eqs. (5.9-5.11) are used.

2. With the left hand side being a derivative with respect to the s variable, this integral is the slope of the parton distribution in the s space. Using this slope, evolve the distribution from s to $s'(= s + \mathrm{d}s)$ by the *predictor-corrector* method.

3. Repeat these steps until the desired s (i.e. Q^2) value is reached.

To speed up the calculations, the program calculates all the function values for the current values of the fit parameters on a predefined $x-s$ space at discrete points, and stores these values in a grid. When a function value for an arbitrary (x, s) value is asked, the result is found and returned by performing a polynomial interpolation of the third order over this grid. Naturally, the grid is recreated when the fit parameters change. This method both considerably reduces the computation time, and due to it's logic, also does provide the extrapolated structure function values for arguments out of the current $x - s$ domain (for instance, extrapolation below $Q^2 < 5$ GeV^2).

5.1.1.3 Target mass correction (TMC)

The evolved structure functions are corrected to account for the target mass effect. Target mass effect occurs in the small Q^2 range, where the approximation that scattering from massless noninteracting quarks is no longer valid. It's the *higher twist* effects which dominate in the low Q^2 region, and introduce terms in the form $ht(x)/Q^{2n}$ in the structure functions, therefore target mass effect is a higher twist effect.

If we define the variable ξ

$$\xi = \frac{2x}{1+k}, \tag{5.12}$$

where

$$k = \left(1 + \frac{4x^2 M_N^2}{Q^2}\right)^{1/2}, \tag{5.13}$$

and the integrals

$$I_1 = \int_\xi^1 du \frac{F_2^{QCD}(u,Q^2)}{u^2}, \tag{5.14}$$

$$I_2 = \int_\xi^1 du \int_u^1 dv \frac{F_2^{QCD}(v,Q^2)}{v^2}, \tag{5.15}$$

$$I_3 = \int_\xi^1 du \frac{xF_3^{QCD}(u,Q^2)}{u^2}, \tag{5.16}$$

then the target mass effect corrected structure functions will be as follows [16]:

$$F_2^{TMC} = \frac{x^2}{k^2}\frac{F_2^{QCD}}{\xi^2} + \frac{6M^2}{Q^2}\frac{x^3}{k^4}I_1 + \frac{12M^4}{Q^4}\frac{x^4}{k^5}I_2, \tag{5.17}$$

$$xF_3^{TMC} = \frac{x^2}{k^3}\frac{xF_3^{QCD}}{\xi^2} + \frac{2M^2}{Q^2}\frac{x^3}{k^3}I_3. \tag{5.18}$$

5.1.2 The fits

In this study, two different fits were made to the CCFR structure function data, the four parameter xF_3-*only fit* and the eight parameter F_2-xF_3 *combined fit*. The advantage of the xF_3-only fit is that the AP equation (1.57) for the nonsinglet distribution does not depend on the gluon distribution $G(x)$, hence is independent of the assumptions and parameterizations made to describe the gluon distribution. On the other hand, the combined fit has the advantage of incorporating the F_2 data to the fit, hence improving the statistical precision of the fit, also providing information about the gluon distribution.

The fits are performed with the χ^2 minimization technique, making use of the `CERNLIB`'s `MINUIT` package [17]. According to this technique, the χ^2 function, which provides a measure of the *goodness of the fit* between a set of experimental data and a model, is tried to be minimized by varying the fit parameters of the model. χ^2 function is defined as following:

$$\chi^2 = \sum_{i,j} (x_i - y_i(a))\, V_{ij}\, (x_j - y_j(a)), \tag{5.19}$$

where x is the vector of observations, y is the vector of model predictions, a is the vector of fit parameter values and V is the inverse of the covariance matrix (also called the error matrix) of the observations x.

In case the observations x are statistically independent from each other, the covariance matrix is diagonal and the expression for χ^2 reduces to the familiar form:

$$\chi^2 = \sum_i \frac{(x_i - y_i(a))^2}{e_i^2}, \tag{5.20}$$

where e_i^2 are the squared errors of the corresponding measurements x_i.

5.2 Fit Results

For the fits, the structure function data satisfying the following conditions are accepted:

- $Q^2 \geq 5$ GeV^2 and $W^2 \geq 10$ GeV^2, in order to avoid the nonperturbative region, where W^2 is the squared invariant mass of the hadronic final state.
- $x < 0.7$, to avoid the region with large Fermi-motion and Monte-Carlo corrections.

Fit results are tabulated in Table 5.1 and the covariance and correlation matrices of xF_3 and combined fits can be found in Tables 5.2-5.4. F_2 and xF_3 structure function data and the QCD fit results for the combined fit are depicted in Figures 5.1 and 5.2, respectively. A plot of the nonsinglet, singlet and gluon distributions as measured by this study can be found in Fig. 5.5.

In Table 5.1, also the Gross-Llewellyn Smith sum rule integral $\int_0^1 F_3 \, \mathrm{d}x$ [18], which gives the number of valence quarks in the nucleon is evaluated with the xF_3 results. As the integrand xF_3/x is singular for $x = 0$, the lower limit of the integral is taken to be '0.0025', instead of taking '0'.

The fit results show that, LO-QCD theory prediction for scaling violations is consistent with the structure function data. The average χ^2/DOF= 1.6 value

Table 5.1: Fit results for the xF_3-only and F_2-xF_3 combined fits of the LO-QCD model to the CCFR structure function data. The reported are 1σ deviation simultaneous statistical errors, and the systematic errors, respectively. Here, DOF corresponds to the *degree of freedom* of the fit, which is the difference of the data points incorporated in the fit and the number of fit parameters in the model: DOF=$n_{data} - n_{fit\,parameters}$. GLS integral is the Gross-Llewellyn Smith sum rule integral, which gives the number of valence quarks in the nucleon.

Parameter	xF_3-only fit	Combined fit
Λ (MeV)	$296\,^{+112}_{-99} \pm 112$	$289\,^{+62}_{-59} \pm 76$
A_{NS}	$7.43 \pm 0.49 \pm 0.34$	$7.85 \pm 0.50 \pm 0.32$
η_1	$0.83 \pm 0.03 \pm 0.01$	$0.86 \pm 0.03 \pm 0.01$
η_2	$3.50 \pm 0.11 \pm 0.16$	$3.58 \pm 0.07 \pm 0.13$
A_S		$1.52 \pm 0.06 \pm 0.07$
η_S		$8.05 \pm 0.38 \pm 0.30$
A_G		$4.11 \pm 0.95 \pm 0.98$
η_G		$3.69 \pm 0.89 \pm 0.50$
χ^2/DOF	128/82	272/164
GLS integral	2.39	2.37
α_s	$0.131 \pm 0.008 \pm 0.008$	$0.131 \pm 0.004 \pm 0.004$

of two fits, which is higher than '1' is due to the QCD model being leading order. The measured values of $\Lambda_{\rm LO}$ from the xF_3-only and the combined fit are consistent with one another. This shows the reliability of the results, specifically the results for the gluon distribution parameters A_g and η_g. Note that the gluon distribution parameters are found from an indirect measurement, from the co-evolution of $G(x, Q^2)$ with F_2 in AP evolution equations.

Statistical errors of the fit parameters shown on Table 5.1 are higher in the xF_3-only fit, compared to the combined fit errors. This is due to the xF_3 structure function data having a higher statistical error compared to F_2, since xF_3 measurement is made from the difference of neutrino and antineutrino events, while the F_2 measurement is made from their sum. As the results from the two fits are consistent, the combined fit result $\Lambda_{\rm LO}= 289\,^{+62}_{-59} \pm 76$ MeV ($\pm$stat. $\pm$syst.) which has a smaller statistical error is reported as the result of this study.

Table 5.2: Covariance matrix of the xF_3-only fit, which is the inverse of the second derivative matrix of the χ^2 function with respect to the fit parameters, evaluated at the χ^2 minimum.

Parameter	Λ	A_{NS}	η_1	η_2
Λ	0.11E-1	0.29E-2	0.66E-3	-0.92E-2
A_{NS}	0.29E-2	0.24E+0	0.14E-1	0.31E-1
η_1	0.66E-3	0.14E-1	0.89E-3	0.14E-2
η_2	-0.92E-2	0.31E-1	0.14E-2	0.13E-1

Table 5.3: Correlation matrix of the xF_3-only fit. In absolute value, increasing values represent increasing correlation, where a value of one represents maximal correlation.

Parameter	Global	Λ	A_{NS}	η_1	η_2
Λ	0.981	1.000	0.055	0.205	-0.768
A_{NS}	0.994	0.055	1.000	0.966	0.570
η_1	0.987	0.205	0.966	1.000	0.406
η_2	0.990	-0.768	0.570	0.406	1.000

The fits were repeated for various Q^2 cuts. The results are tabulated in Table 5.6. From the results, it's seen that the Q^2 cuts do affect the measured $\Lambda_{\rm LO}$ values. The $Q^2 > 1$ cut results in a poor fit, this is due to the inclusion of the data belonging to the non-perturbative region, which cannot be predicted in the context of PQCD. In this region, also the target mass correction loses it's validity. Nonetheless, note that the $\Lambda_{\rm LO}$ result of this fit is almost the same as the result found for the $Q^2 > 5$ cut.

The higher Q^2 cuts suggest higher values for $\Lambda_{\rm LO}$ along with decreased χ^2/DOF ratios. This interesting result can be understood by checking the α_S^{LO} and α_S^{NLO} vs. Q^2 plots, see Fig. 1.3. The NLO running coupling constant is lower than the LO coupling, and their difference diminishes as $Q^2 \to \infty$. However from this plot we note that, decrease in their difference is quite large for lower values of Q^2. In other words, with increasing Q^2, α_s^{LO} becomes closer to the NLO coupling. The increase in the measured $\Lambda_{\rm LO}$ values and decrease in the χ^2/DOF ratios can be understood within this context. The LO-coupling

Table 5.4: Covariance matrix of the combined fit.

Parameter	Λ	A_{NS}	η_1	η_2	A_S	η_S	A_G	η_G
Λ	0.37E-2	0.20E-2	0.19E-3	-0.23E-2	0.61E-3	0.74E-2	-0.25E-1	-0.26E-01
A_{NS}	0.20E-2	0.25E+0	0.15E-1	0.29E-1	0.17E-1	0.81E-1	0.17E-1	0.19E-1
η_1	0.19E-3	0.15E-1	0.91E-3	0.16E-2	0.10E-2	0.36E-2	0.14E-2	0.16E-2
η_2	-0.23E-2	0.29E-1	0.16E-2	0.54E-2	0.17E-2	0.61E-2	0.13E-1	0.13E-1
A_S	0.61E-3	0.17E-1	0.10E-2	0.17E-2	0.33E-2	0.16E-1	-0.22E-1	-0.19E-1
η_S	0.74E-2	0.81E-1	0.36E-2	0.61E-2	0.16E-1	0.14E+0	-0.97E-1	-0.16E+0
A_G	-0.25E-1	0.17E-1	0.14E-2	0.13E-1	-0.22E-1	-0.97E-1	0.99E+0	0.75E+0
η_G	-0.26E-1	0.19E-1	0.16E-2	0.13E-1	-0.19E-1	-0.16E+0	0.75E+0	0.80E+0

Table 5.5: Correlation matrix of the combined fit.

Parameter	Global	Λ	A_{NS}	η_1	η_2	A_S	η_S	A_G	η_G
Λ	0.969	1.000	0.066	0.102	-0.511	0.175	0.320	-0.409	-0.483
A_{NS}	0.997	0.066	1.000	0.967	0.788	0.594	0.422	0.034	0.042
η_1	0.993	0.102	0.967	1.000	0.708	0.593	0.313	0.045	0.059
η_2	0.989	-0.511	0.788	0.708	1.000	0.389	0.217	0.176	0.195
A_S	0.932	0.175	0.594	0.593	0.389	1.000	0.710	-0.377	-0.364
η_S	0.955	0.320	0.422	0.313	0.217	0.710	1.000	-0.258	-0.485
A_G	0.941	-0.409	0.034	0.045	0.176	-0.377	-0.258	1.000	0.838
η_G	0.957	-0.483	0.042	0.059	0.195	-0.364	-0.485	0.838	1.000

which becomes closer to the NLO coupling yields a better χ^2/DOF ratio and an increased $\Lambda_{\rm LO}$ value. Note that the NLO measurements yield higher values of Λ than the LO studies. This is due to the coupling being an increasing function of Λ, hence the decrease in the coupling when we get from LO to NLO is compensated by an increase in this quantity.

Can this result be interpreted as a suggestion for a higher Q^2 cut? Checking the plots of the logarithmic slopes of the fits with $Q^2 > 10, 15$ states that the answer is no. From these plots it's seen that the predicted slopes of the model for these cuts are not consistent with the slopes predicted by the data, especially in the high-x region. The effect of a higher Λ value on the logarithmic slopes can be seen in Fig. 5.3. In the next section where the logarithmic slopes of the structure function data and the QCD-model are compared, it will be deduced that the QCD parameter Λ is mainly determined by the high-x data. Therefore, although yielding results consistent with the structure function data in the low and medium x ranges, fits with the higher Q^2 cuts give results inconsistent with the data in the high-x region, suggesting $Q^2 > 5$ as a convenient cut, both excluding the nonperturbative region, and including the data set for obtaining a reliable measurement of $\Lambda_{\rm LO}$. In fact this result reflects a fact we already know. It's normal that a parameter drawing the border between the internal world of

Table 5.6: QCD fit results for various Q^2 cuts. Higher cuts suggest higher values of $\Lambda_{\rm LO}$ and lower χ^2/DOF ratios.

Q^2 Cut	$\Lambda_{\rm LO}$	χ^2/DOF
$Q^2 > 1$	290 ± 40	$537/212\,(2.5)$
$\mathbf{Q^2 > 5}$	$\mathbf{289 \pm 61}$	$\mathbf{272/164\,(1.7)}$
$Q^2 > 10$	297 ± 69	$170/118\,(1.4)$
$Q^2 > 15$	342 ± 92	$122/92\,(1.3)$

the nucleon and the world of hadrons is determined by low-Q^2 and high-x data, as these data correspond to the proximity of this border.

The systematic errors of the fit parameters are calculated by repeating the fits by using the structure function data samples shifted by $\pm 1\sigma$ deviations with the systematic errors reported for the data. This procedure is performed for each of the 18 systematic error sources. Deviations in the fit parameters for $-\sigma$ and $+\sigma$ shifts of the data are averaged, then the average values are added in quadrature to yield the total systematic error.

Results of the systematic error study for Λ can be found in tables 5.7 and 5.8. In these tables, the negative average values emphasize that the Λ has decreased for a $+\delta$ shift of the data sample with the error corresponding to the particular systematic effect. From the results, it can be seen that the dominant systematic effect is the muon energy calibration C_μ for both fits. It can also be seen that the combined fit is less sensitive to the systematic effects compared to the xF_3-only fit.

5.3 Logarithmic Slopes

Calculation of the logarithmic slopes $\frac{\mathrm{d}\ln F_i}{\mathrm{d}\ln Q^2}$ for the structure function data and the QCD model provides a good means of checking the agreement between the data and the QCD model. The logarithmic slopes of the structure function data are found by fitting each x-bin of the structure function data to the following Q^2 parameterization:

$$F_i(Q^2) = A \times (Q^2)^C, \tag{5.21}$$

Table 5.7: Systematic error analysis results of the xF_3-only fit, for Λ. The base value is $\Lambda = 296$ MeV ($\chi^2 = 128$). The average is the average of the $+\sigma$ and the $-\sigma$ shifts, in absolute value. Total systematic error is calculated by adding the individual contributions in quadrature. Note that some error sources do not have a negative shift.

	$-\sigma$ shift		$+\sigma$ shift		
Source	Λ	χ^2	Λ	χ^2	Average
C_{HAD}^{744}	35	134	-34	126	-35
C_{HAD}^{770}	37	126	-36	134	-36
ΔE_{HAD}	20	130	-20	126	-20
C_μ	-66	141	68	134	67
ΔE_μ	9	127	-9	131	-9
$(B/A)_{744}^{\nu}$	-18	132	18	124	18
$(B/A)_{770}^{\nu}$	-22	133	22	123	22
$(B/A)_{744}^{\bar{\nu}}$	4	126	-4	129	-4
$(B/A)_{770}^{\bar{\nu}}$	6	125	-6	130	-6
σ^{ν}/E	0	122	0	133	0
$\sigma^{\bar{\nu}}/\sigma^{\nu}$	42	123	-40	135	-41
No Φ Adj.	–	–	-16	136	-16
R	0	128	0	128	0
m_c	–	–	-11	143	-11
κ	–	–	-20	137	-20
α	–	–	-16	136	-16
B_c	–	–	-21	137	-21
Model Parameterization	–	–	23	134	23
					Total Systematic Error: 112

where A and C are the fit parameters. It's easy to notice that the logarithmic slope is nothing but the fit parameter C:

$$\frac{\mathrm{d}\ln F_i(Q^2)}{\mathrm{d}\ln Q^2} = C \tag{5.22}$$

The logarithmic slopes of F_2 and xF_3 are depicted in Figs. 5.3 and 5.4, using the parameter results of the combined fit. For both structure functions, the logarithmic slopes of the structure function data and the QCD model are in agreement. In Fig. 5.3, also plotted are the slopes of the model prediction for F_2 with $\Lambda_{\mathrm{LO}}\pm100$ MeV. From this plot, it can be seen that Λ_{LO} is mainly

Table 5.8: Systematic error analysis results of the combined fit for Λ. The base value is $\Lambda = 289$ MeV ($\chi^2 = 272$). Note that some error sources do not have a negative shift.

	$-\sigma$ shift		$+\sigma$ shift		
Source	Λ	χ^2	Λ	χ^2	Average
C_{HAD}^{744}	23	285	-23	267	-23
C_{HAD}^{770}	28	276	-28	278	-28
ΔE_{HAD}	18	284	-17	262	-18
C_μ	-43	304	44	283	43
ΔE_μ	1	272	-1	277	-2
$(B/A)_{744}^{\nu}$	-8	275	8	269	8
$(B/A)_{770}^{\nu}$	-9	276	9	268	9
$(B/A)_{744}^{\bar{\nu}}$	0	270	0	273	0
$(B/A)_{770}^{\bar{\nu}}$	0	269	0	274	0
σ^{ν}/E	0	260	0	283	0
$\sigma^{\bar{\nu}}/\sigma^{\nu}$	-6	274	6	276	6
No Φ Adj.	–	–	-6	287	-6
R	0	266	0	277	0
m_c	–	–	0	296	0
κ	–	–	-8	285	-8
α	–	–	-8	288	-8
B_c	–	–	-8	289	-8
Model Parameterization	–	–	21	288	21
					Total Systematic Error: 76

determined by the high-x data.

Inspecting the AP equations (1.55) and (1.57) we note that for a particular value of x, the integrands on the right hand side should vanish. The plots verify this prediction, the slope of xF_3 vanishes for $x \approx 0.10$ and the slope of F_2 vanishes for $x \approx 0.12$.

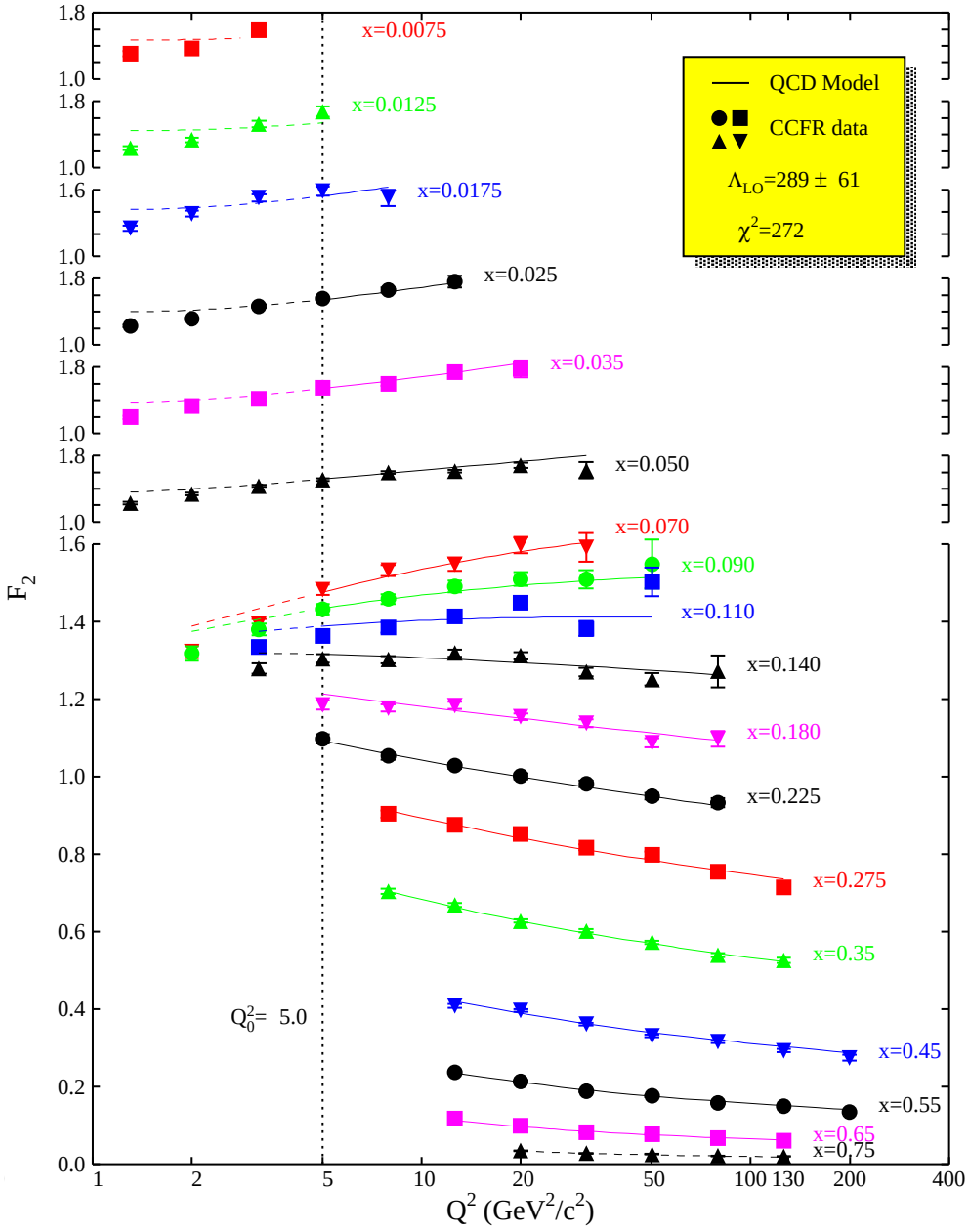

Figure 5.1: Combined fit results for F_2. Dashed lines represent extrapolation of the model.

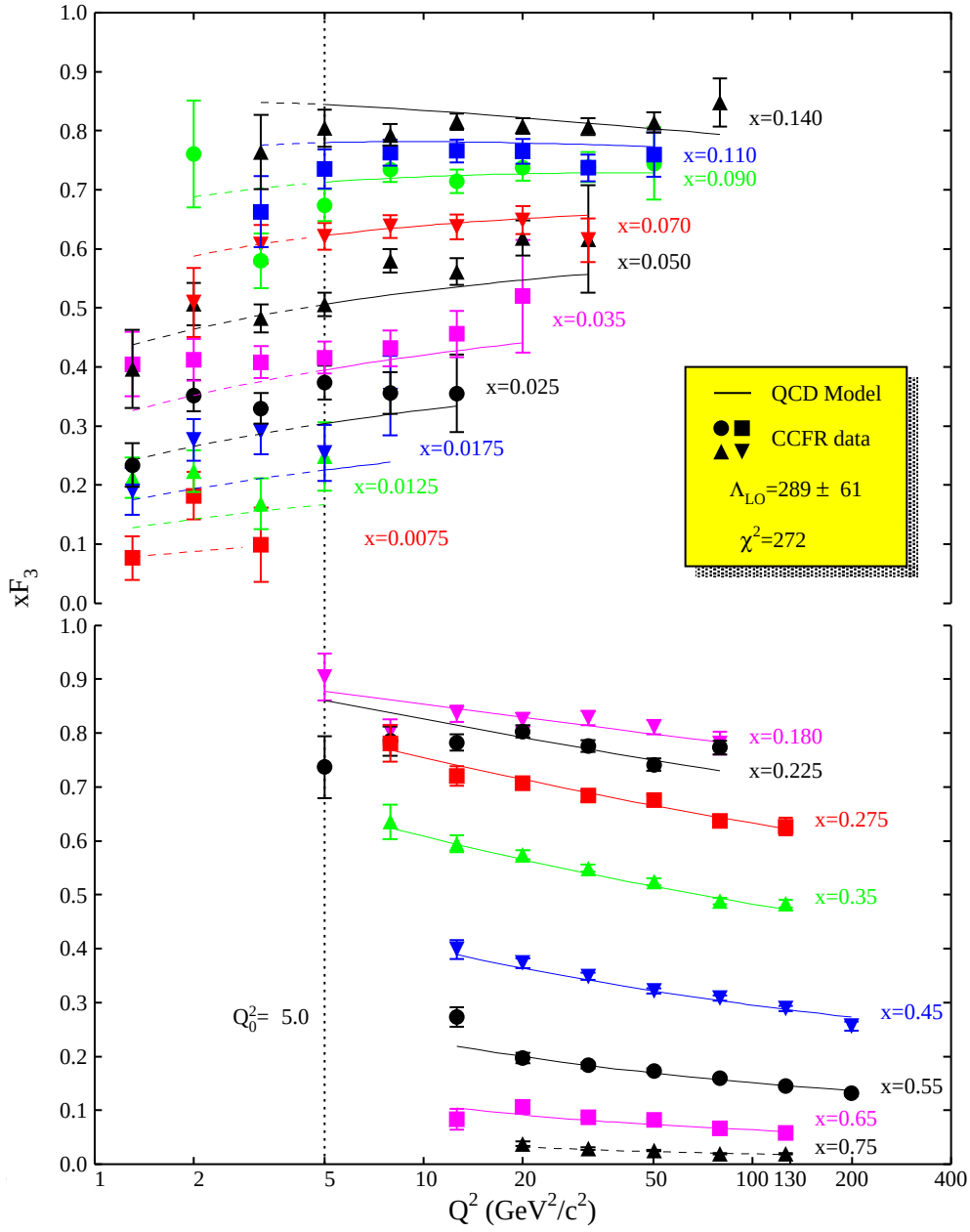

Figure 5.2: Combined fit results for xF_3. Dashed lines represent extrapolation of the model.

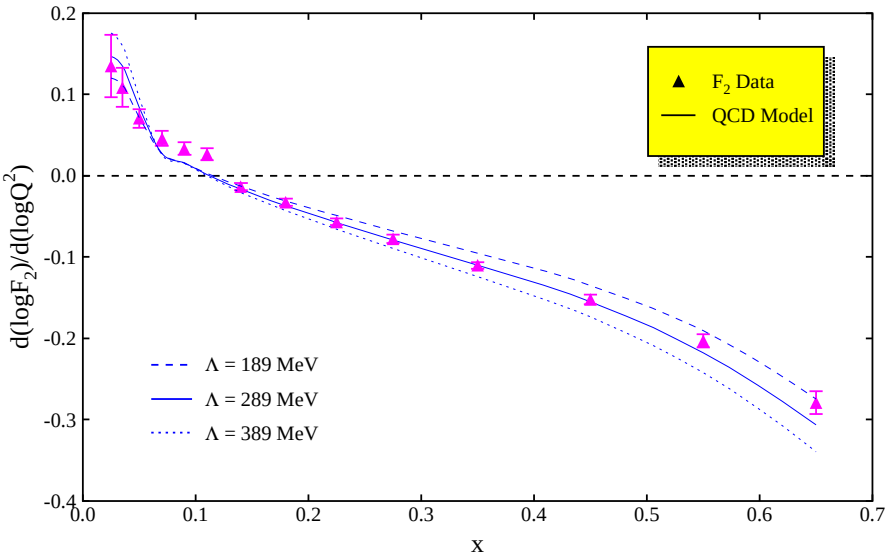

Figure 5.3: Logarithmic slopes of F_2.

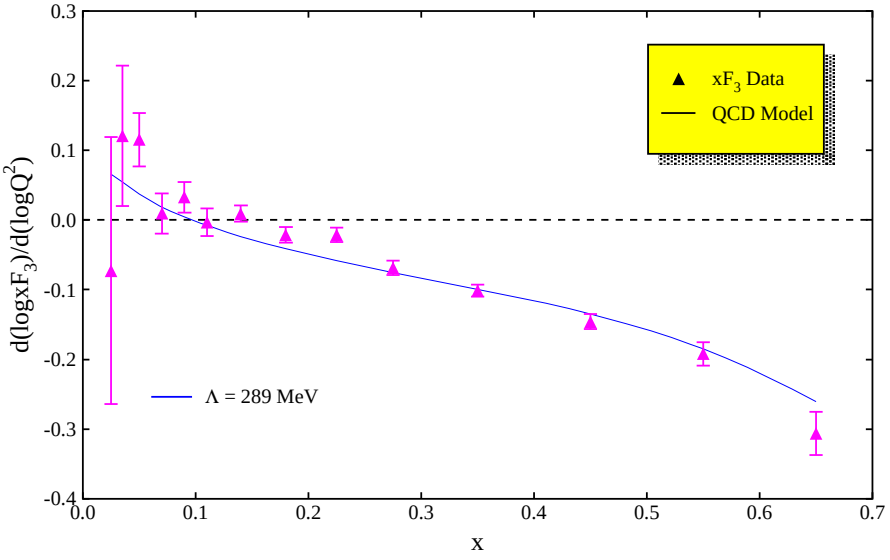

Figure 5.4: Logarithmic slopes of xF_3.

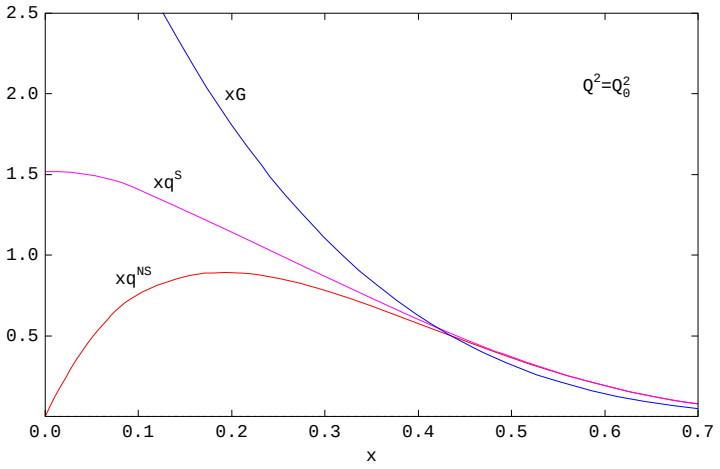

Figure 5.5: The parton distributions as measured in this thesis: $xq^{NS} = xq_v$, $xq^S = x(q + \bar{q})$ and xG. The distributions are reported for $Q^2 = Q_0^2 = 5$ GeV^2. All distributions vanish for $x = 1$, as in this limit the observed entity is the target nucleon itself, as a whole. The sea quark domination as $x \to 0$ determines the vanishing of the nonsinglet distribution. In this limit, the singlet distribution takes a finite value, since this distribution includes contributions from the sea quark distributions. The gluon distribution, which is measured as $xG(x, Q_0^2) = (4.11 \pm 1.36)(1 - x)^{3.69 \pm 1.02}$, also converges to a finite value in this limit.

5.4 Comparisons

Measurement results for the QCD parameter Λ from various experiments are tabulated in Table 5.9 for comparison. All the quoted values are found by direct integrations of the AP evolution equations.

The CDHS experiment [19] studied the deep-inelastic interactions of neutrinos on iron. The tabulated results were found by a computer program developed by Abbott and Barnett [20]. This program uses initial parameterizations for q^S, xq^{NS} and xG very similar to the parameterization used in this study. The quoted LO value is found by a singlet analysis which combined the F_2 and $\bar{q}$ data, assuming $R_{\rm QCD}$. The NLO value is found by a nonsinglet analysis by subtracting the sea quark distribution from the F_2 data and assuming $R \sim 0$.

The CHARM experiment studied neutrino scattering with the nucleons of the marble ($CaCo_3$) target calorimeter. The leading order [21] and the next-to leading order [22] results are calculated by a program developed by Furmanski and Petronzio [23]. The method of the program is based on the expansion of parton distributions in a series of Laguerre polynomials in the variable $y = \ln(1/x)$. The Laguerre polynomials have the advantage of converging quickly, hence the series can be truncated after a few terms with high accuracy. This method also do not require an initial parameterization of parton distribution functions. The quoted LO value was extracted by a singlet analysis using the

Table 5.9: Measurements of the QCD parameter Λ quoted from various neutrino experiments, with corresponding statistical errors. Except the BEBC measurement, the values are extracted for $n_f = 4$. Here $\Lambda_{\overline{\rm MS}}$ refers to a NLO measurement in the modified minimal-subtraction renormalization scheme.

Experiment	Q^2Range (GeV^2)	$\Lambda_{\rm LO}$ (MeV)	$\Lambda_{\overline{\rm MS}}$ (MeV)
CDHS	1-180	290 ± 30	300 ± 80
CHARM	3-78	$190\ ^{+70}_{-40}$	310 ± 150
CCFR 616/701	1-200	300 ± 100	340 ± 110
BEBC	1.5-55	180 ± 60	–
Average:		233	317
CCFR 744/770	1.3-200	$289\ ^{+62}_{-59}$	381 ± 23

F_2 and $\bar{q}$ data. The NLO value was found from xF_3 by a nonsinglet analysis.

The quoted results from the CCFR 616/701 (CCFRR) experiment [24] were found by a program developed by Duke and Owens [25]. Both results were found by singlet analyses.

The BEBC experiment consists of a measurement of nucleon structure functions from neutrino interactions on deuterium. In their nonsinglet $\Lambda_{\rm LO}$ analysis [26] made for $n_f = 3$, to improve statistical accuracy the F_2 data was used in the range $x > 0.4$ instead of the xF_3 data, since in this region $F_2 \approx xF_3$. The BEBC structure function measurements were made with the assumption $R = 0$.

The QCD parameter measurement result $\Lambda^{(4)}_{\rm LO} = 289\,^{+62}_{-59} \pm 76$ MeV for four quark flavors of this study is higher than the previous measurements, and from their average, however the measurement is consistent with them within the quoted errors.

The NLO result of the CCFR experiment is quoted from [15]. This study was made with a modified form of the Duke and Owens program, which uses the same parameterization with this study for the initial parton distributions at Q_0^2. In addition to the standard systematical analysis, CCFR collaboration performed a global systematic fit, which incorporates the systematic effects in the fit. The result of this fit is $\Lambda_{\overline{\rm MS}} = 337 \pm 28$ MeV, obtained from a combined fit of both F_2 and xF_3. This result constitutes the most precise measurement of $\Lambda_{\overline{\rm MS}}$.

From a comparison of the $\Lambda_{\rm LO}$ and $\Lambda_{\overline{\rm MS}}$ values extracted from the same experimental data, one notices that in all cases $\Lambda_{\rm LO}$ is less than $\Lambda_{\overline{\rm MS}}$, which is also suggested by the average values of these measurements. The difference depend on the experiment, it's 10 MeV for CDHS, 120 MeV for CHARM and 40 MeV for CCFRR. The results of this study is also consistent with this picture, the difference with the NLO measurement is 92 MeV, and the difference with the result of the global systematic fit is 48 MeV.

5.5 Conclusion

In this thesis a leading-order QCD analysis of the CCFR structure function data is performed. The QCD parameter $\Lambda_{\rm LO}$ is measured by two methods. The *nonsinglet fit* uses only the xF_3 data, and is independent of the gluon distribution. The *combined fit* uses the F_2 and xF_3 data simultaneously, with increased number of fit parameters. Since the amount of data entering the combined fit is doubled, and the F_2 data have a higher precision than the xF_3 data, this analysis has a statistical advantage over the xF_3-only fit, yielding results with higher statistical precision. In the combined fit, the gluon distribution is co-evolved with the singlet distribution, hence this fit also provides information about the gluon distribution.

The nonsinglet analysis yielded a value $\Lambda_{\rm LO}= 296\,^{+112}_{-99} \pm 112$ MeV and the singlet analysis yielded $\Lambda_{\rm LO}= 289\,^{+62}_{-59} \pm 76$ MeV. The results were found to be consistent, hence the value with smaller statistical error, $\Lambda_{\rm LO}= 289\,^{+62}_{-59} \pm 76$ MeV is reported as the result of this study. This value corresponds to a measurement of the strong coupling constant, $\alpha_s(M_Z^2) = 0.131 \pm 0.004 \pm 0.004$. Comparisons show that the $\Lambda^{(4)}_{\rm LO}$ value found in this analysis is comparable to the world-wide measurements of this parameter.

REFERENCES

[1] F. Halzen, A. D. Martin, *Quarks and Leptons: An Introductory Course in Modern Particle Physics*, 1984.

[2] J. I. Friedman, *et al.*, Rev. Mod. Phys. **63**, 573,597,615 (1991).

[3] C. G. Jr. Callan and D. J. Gross, Phys. Rev. Lett. **22**, 156 (1969).

[4] J. D. Björken, Phys. Rev. **179**, 1547 (1969).

[5] R. P. Feynman, Phys. Rev. Lett. **23**, 1415 (1969).

[6] I. J. R. Aitchson, A. J. G. Hey, *Gauge Theories in Particle Physics*, 1989.

[7] G. Altarelli, G. Parisi, Nucl. Phys. B **126**, 298 (1977).

[8] W. G. Seligman, Ph.D. Thesis (Columbia University), Nevis Report No 292, 1997.

[9] U. K. Yang, Ph.D. Thesis (University of Rochester), 2001.

[10] A. J. Buras, K. J. F. Gaemers, Nucl. Phys. B **132**, 249 (1978).

[11] M. Gluck, *et al.* (GRV Collaboration), Z. Phys. C **67**, 433 (1995).

[12] L. W. Whitlow, *et al.*, Phys. Lett. B **250**, 193 (1990).

[13] D. Yu. Bardin, V. A. Dokuchaeva, JINR-E2-86-260 (1986).

[14] S. A. Rabinowitz, *et al.* (CCFR Collaboration), Phys. Rev. Lett. **70**, 134 (1993).

[15] W. G. Seligman *et al.*, Phys. Rev. Lett.**79**, 1213 (1997).

[16] H. Georgi, H. G. Politzer, Phys. Rev. D **14**, 1829 (1976).

[17] F. James and M. Goosens; *MINUIT, Function Minimization and Error Analysis*; CERN Program Library Entry **D506**, (1994).

[18] D. J. Gross and C. H. Llewellyn Smith, Nucl. Phys. B **14**, 337 (1969).

[19] CDHS Collab., H. Abramovicz *et al.*, Z. Phys. C **17**, 237 (1983).

[20] L. F. Abbott and R. M. Barnett, Ann. Phys. **125**, 289 (1980).

[21] Charm Collab., F. Bergsma *et al.*, Phys. Lett. B **123**, 269 (1983).

[22] Charm Collab., F. Bergsma *et al.*, Phys. Lett. B **153**, 111 (1985).

[23] W. Furmanski and R. Petronzio, Z. Phys. C **11**, 293 (1982).

[24] D. B. Mac Farlane *et al.*, Z. Phys. C **26**, 1 (1984).

[25] A. Devoto *et al.*, Phys. Rev. D **27**, 508 (1983).

[26] D. Allasia *et al.*, Z. Phys. C **28**, 321 (1985).

Index